Numerical Investigation of V/STOL Jet Induced Interactions*

Magdi H. Rizk and Suresh Menon

Flow Industries, Inc.

Abstract

Direct numerical simulation using the full three-dimensional, time-dependent Navier-Stokes equations is used to investigate V/STOL jet induced interactions. The objective of this numerical simulation is to compute accurately the details of the flow field and to achieve a better understanding of the physics of the flow, including the role of initial turbulence in the jet, the influence of forward motion on hover aerodynamics, the collision zone and fountain characteristics. Preliminary results are presented.

1. Introduction

The fluid dynamics of impinging jets of V/STOL aircraft is complex, to say the least. The complexity is compounded by compressibility, combustion and heat transfer, as well as complex interactions between airframe and ground, forward flight, oblique impingement, jet turbulence, jet exit profile shape, etc. Clearly, an accurate prediction of the aerodynamic forces and moments on the aircraft is not possible without understanding the associated flow physics.

V/STOL aircraft have different operating modes (hovering and transition in and out of ground effect). The flow fields associated with these modes of operation are substantially different. Many of the complex flow phenomena associated with these flow fields are poorly understood, thereby restricting our ability to optimize the aircraft design. Lifting jets entrain air, which leads to induced suction pressures on the aircraft lower surface. When the aircraft is hovering near the ground, further entrainment is caused by the wall jets (associated with the ground). This significantly increases the suckdown force on the aircraft. The problem becomes more complex in the case of multiple jets. Here the wall jets collide and form a fountain that impinges on the aircraft undersurface. While this impingement creates an upload, which partly offsets the suckdown force, the fountain flow causes further reduction in the pressure between the jets and the fountain. The complex flow fields associated with multiple jets in ground effect are also not well understood.

Presently, experimental work is the main avenue followed to gain an understanding of flows associated with V/STOL aircraft. However, such studies have addressed mostly global features and time-averaged measurements of impinging jets. Experiments in this configuration are extremely cumbersome, and measurements are crude and inaccurate owing to the flow being turbulent, globally unsteady and three-dimensional. Characterization of this flow will require measurements involving three-dimensional arrays of sensors. These sensors (hot-wires, for example) have the constraints that they cannot discriminate flow reversal from forward flow and are prone to probe interference. An array of LDAs would be prohibitively expensive.

Numerical simulation provides the opportunity of studying the detailed flow physics as a function of space and time. Although the complete flow field around a V/STOL aircraft will be difficult to solve today, because of the size limitation of present-day computers, some local flow domains, such as the impinging jet flow, can be studied. The simulation can be either a direct numerical simulation or a large-eddy simulation (LES) involving subgrid-scale modeling. In fact, numerical simulation provides a number of advantages: it provides the instantaneous distribution of all flow variables over the entire three-dimensional flow field considered; it allows "measurements" of flow properties not possible experimentally (for example, pressure within turbulent flows); it can provide simultaneous "flow visualization" and "measurements" in arbitrary planes.

Numerical experimentation is often more desirable than laboratory experimentation, because the former allows independent control of the flow parameters or any choice of arbitrary combinations of parameter values. Such independent control or arbitrary combination is difficult in any apparatus. Similarly,

162

variations of parameters like initial conditions, free-stream turbulence, excitation frequency, excitation amplitude, etc., can be typically more easily introduced in numerical experiments than in laboratory experiments.

The majority of the research work directed towards investigating V/STOL flows has been experimental. Only within the past few years have sufficient advances in computer capabilities made it feasible to attempt numerical simulation of the three-dimensional viscous equations for the V/STOL related flow fields. With present computer capabilities numerical simulations cannot replace experimental procedures. However, they can complement experimental efforts in gaining a deeper understanding of the complex flow phenomena associated with V/STOL flows. The design and analysis of traditional aircraft components have benefitted greatly from numerical computations. Computational methods are expected to have a similar impact on V/STOL problems.

The computational work initially was limited to solving two dimensional problems. Using an incompressible inviscid rotational flow model, Rubel (1978) investigated the normal impingement of axisymmetric jets and the oblique impingement of two-dimensional jets upon a flat surface. This model was then extended to allow three-dimensional computations (Rubel, 1981). Kotansky and Bower (1978) investigated planar turbulent jet impingement. They solved the time-averaged Navier-Stokes equations using a one-equation turbulence model. In this approach, it was necessary to specify the turbulence length-scale distribution. To avoid this disadvantage, Agarwal and Bower (1982) replaced the one-equation turbulence model by the two-equation (k-ϵ) turbulence model. The work of Kotansky and Bower (1978) was extended to solve the problem of three-dimensional lift jets in ground effect by Bower et al. (1979). This work was the first attempt to calculate interacting jets with fountain formation. Computer limitations restricted the calculations to a relatively coarse computational mesh and to low Reynolds number. More, recently Childs and Nixon (1985) solved the impingement problem for three-dimensional jets using the time-averaged Navier-Stokes equations in conjunction with the two-equation (k-ϵ) turbulence model.

Work is in progress at Flow Industries on the direct numerical simulation of complex V/STOL flows using the full three-dimensional, time-dependent Navier-Stokes equations. The objective of this numerical simulation is to compute accurately the details of the flow field and to achieve a better understanding of the physics of the flow, including the role of initial turbulence in the jet, the influence of forward motion on hover aerodynamics, the collision zone and fountain characteristics. The computational tools necessary have been partially developed. Preliminary calculations have been performed using a relatively coarse computational mesh for a low Reynolds number flow. The results presented here are not intended to be an accurate simulation of V/STOL flow configurations. Nevertheless, they do indicate the main features of these flows.

2. Approach

In turbulent flows, there is a wide range of spatial and temporal scales. The separation between the largest and the smallest scales of motion widens as the Reynolds number increases. For V/STOL flows, the numerical resolution of all relevant scales of motion is impossible. Modeling of some aspects of the flow is therefore necessary. In the classical approach, based on Reynold's ideas for solving turbulent flow problems, the Navier-Stokes equations are averaged. All fluctuations are modeled, and only mean flow variables are calculated. This approach has been used by various researchers but has met with only limited success. In the V/STOL problem, different flow regions exist in which the large-scale structures vary greatly from one to another. It is therefore difficult to model the large-scale structures. To avoid this difficulty, the large-eddy simulation (LES) approach is followed here. In this approach, the large scales, containing most of the turbulent energy and providing most of the important turbulent transport, are explicitly calculated. The small-scale turbulence structures, which are nearly isotropic and universal in character, are modeled in a simple, relatively crude manner. Furthermore, LES can be used to investigate the temporal development of the flowfield. This allows us to study a broader range of problems relevant to V/STOL flows, e.g., the unsteady separation in boundary layers produced by impinging jets (Didden and Ho, 1985), the evolution of large, spatially coherent structures in the jet (Crow and Champagne, 1971) and the different stability modes in the jet (Strange and Crighton, 1983).

The governing equations that are numerically solved are the full Navier-Stokes equation for incompressible flow. When the Reynolds number is too large to resolve numerically the entire range of energetic scales, filtering is used to eliminate the smaller (subgrid-scale) motions. Filtering introduces new terms, similar to Reynolds stress terms obtained in the Reynolds-averaged equations, that contain the effect of subgrid-scale motions on the numerically resolved motions. These subgrid Reynolds stresses can be modeled using an eddy viscosity (see Moin and Kim, 1982).

The finite difference approximations to the governing equations are written at the mesh points of a staggered grid (Harlow and Welch, 1965). The pressure is determined at each time step by solving the governing Poisson equation. Efficient methods for the direct solution of the discrete Poisson equation are used (Buzbee et al., 1970). The Adams-Bashforth scheme is used to advance the velocity in time.

The problem under investigation is that of an infinite row of jets impinging on the ground (see Figure 1). This problem, which contains the essential features of twin jets impinging on the ground (see Figure 2), simulates the hovering configuration. The jets may be inclined in the y direction, which leads to a configuration associated with an aircraft in pitch while hovering. By imposing a cross flow in the y direction, it is possible to study the effects of the aircraft's forward motion during takeoff and transition.

A computer code that solves the time-dependent Navier-Stokes equations has been developed with the purpose of numerically simulating the problem of an

infinite row of jets impinging on the ground. Subgrid-scale modeling, which would allow the solution of problems at higher Reynolds numbers is currently being introduced into the code. Although the code is not in its final form, it has been used to obtain solutions that indicate the main feature of V/STOL aerodynamics.

3. Numerical Results

The results presented here are preliminary examples that have been solved using the code in its present form. A relatively coarse numerical mesh was used, and the Reynolds number was assumed to be low enough so that filtering was not required. The results presented here are not intended to be an accurate simulation of V/STOL flow configurations. Nevertheless, the results of the steady-state examples presented here indicate the main features of the impinging jet flow. The unsteady behavior of the jet flow due to forcing at a specific frequency has also been investigated.

3.1 Steady-State Calculations

The following three examples indicate some of the main features of V/STOL flows. In these examples the plane $x = x_j$ (see Figure 1) is assumed to be a plane of symmetry and, unless otherwise stated, the computational domain is defined by

$$0 = x_j \leq x \leq x_f = 1$$
$$-2 = y_B \leq y \leq y_b = 2$$
$$0 = z_g \leq z \leq z_a = 1$$

where all dimensions are normalized by the jet diameter. The jet velocity profile in the direction of the jet axis is assumed to be given by

$$Q_j(r) = 1 - \frac{r^2}{R_j^2} \qquad (1)$$

where R_j is the jet radius, r is the distance from the jet axis, and velocities are normalized by the maximum jet velocity. The Reynolds number in these examples is based on the jet diameter and the maximum jet velocity.

Example 1:

In this example, the jet axis is normal to the ground plane ($\alpha = 90°$) and there is no crossflow ($V = 0$). The jet at a Reynolds number (Re) of 300 is solved in a 18x72x18 (x,y,z) mesh.

Figures 3 through 9 show the main features of the flow generated by a row of vertical jets impinging on the ground. The velocity vectors in the planes $x = x_j$ and $x = x_f$ are shown in Figures 3 and 4, respectively. The fan-shaped fountain that results from the collision of the two wall jets is apparent in Figure 4. The jet, the wall jet, and the fountain can be seen in Figure 5. Figures 6

through 9 show the pressure contours that indicate high-pressure areas in the zones of jet-ground impingement, wall jet-wall jet collision, and fountain impingement on the upper boundary.

Example 2:

In this example the jet axis is inclined at an angle $\alpha = 60°$ to the ground. A crossflow of $V = 0.2$ is imposed on the flow field. The Reynolds number and mesh size is the same as in Example 1.

Figures 10 through 13 show the main features of the flow generated by a row of inclined jets impinging on the ground in a crossflow. In Figure 10 the ground vortex formed by the interaction of the crossflow and the wall jet is apparent. The effect of the crossflow on the fan-shaped fountain is shown in Figure 11, where it is no longer symmetric.

For the problem of a jet in a crossflow, two basic configurations are relevant to V/STOL aerodynamics. In the first configuration, the jet impinges on the ground. The main features of this flow are indicated in Example 2. A second configuration results as the distance between the aircraft and the ground becomes large and/or as the forward aircraft speed becomes large. In this case, the jet does not impinge on the ground. This configuration is shown in the following example.

Example 3:

In this example $\alpha = 90°$, $V = 0.7$, and $Re = 60$. A 7x28x14 mesh is used. The computational domain is defined by

$$0 = x_j \leq x \leq x_f = 1$$
$$-2 = y_B \leq y \leq y_b = 2$$
$$0 = z_g \leq z \leq z_a = 2.$$

Figures 14 through 18 show the main features of this flow. Figure 14 indicates that the jet changes its direction before it reaches the ground. As indicated in Figure 15, no fountain flow develops in this example since there are no wall jets. The double vortex generated by the jet-crossflow interaction is shown in Figure 16. As indicated by the pressure contours shown in Figure 17, a high-pressure region develops upstream of the jet, while a low-pressure region develops downstream of the jet in its wake. Figure 18 shows the vorticity distribution in the y-z plane.

To investigate the effect of different inflow jet velocity profile on the jet development, a series of steady-state calculations was carried out. Four different initial jet profiles were investigated: the r^n-profiles (where $n = 2,4,6$) and the tanh-profile. The computational domain and grid resolution were kept the same with the ground plane at $H/D = 8$, where H is the distance between the upper and lower walls while D is the jet exit diameter. This is in contrast to the steady-state calculations (Examples 1-3) where the ground plane was kept much closer to the jet exit. In this study, the ground plane was kept as far away as possible so that the jet development and stability

would not be directly affected by the resonance effect of the ground plane. The basic thrust of these steady-state calculations was to investigate numerically the experimental observation that the flatter profiles (e.g., tanh, top-hat) are inherently more unstable than the less flat profiles (e.g., parabolic). This experimentally observed instability has been attributed mainly to the initial shear layer instability, which is more pronounced for the broader profile (due to the thinness of the initial shear layer). However, to observe numerically the shear layer instability, a very high grid resolution is required near the jet lip, which at present is not possible due to computational limitations. Furthermore, to obtain accurate results with the available grid resolution, the Reynolds number and the computational domain had to be kept small, which is another limitation inherent in these calculations. However, we expected that there are other overall features of the jet development that will show the effect of varying the jet profile; the present steady-state calculations were directed towards determining these effects.

In the following, we present the steady-state solutions obtained for the different jet velocity profiles. We have assumed that the flow field is symmetric in the x-direction and, therefore, only the half-plane (with respect to the y-axis) is shown. The grid used in all these calculations is a 16x32x64 mesh, and the computational domain is defined as

$$
\begin{aligned}
0 &\leq x/D \leq 1 \\
-2 &\leq y/D \leq 2 \\
0 &\leq z/D \leq 8
\end{aligned}
\tag{2}
$$

The ground plane is located eight jet diameters ($H/D = 8$) below the jet exit plane, and a uniform grid distribution is used in the whole computational domain. The jet velocity profiles are given by

$$
\begin{aligned}
\text{Profile I:} \quad & w_j = w_{jo}(1 - \eta^2) \\[6pt]
\text{Profile II:} \quad & w_j = w_{jo}(1 - \eta^4) \\[6pt]
\text{Profile III:} \quad & w_j = w_{jo}(1 - \eta^6) \\[6pt]
\text{Profile IV:} \quad & w_j = \frac{w_{jo}}{2} \left\{1 + \tanh\left[b\left(\frac{1}{\eta} - \eta\right)\right]\right\}
\end{aligned}
\tag{3}
$$

where $\eta = r/R$, R is the radius of the jet, and w_{jo} is the reference velocity, taken to be unity at the centerline of the jet. Here $b = 2R/\delta$, where δ is the momentum thickness. We took $b = 25/16$, from Strange and Crighton (1983) which is an empirical fit to Crow and Champagne's (1971) data two jet diameters below the exit plane.

In the following discussion, the velocity profiles given by Equation (3) will be identified as Profiles I through IV. Profile I is the parabolic profile, and Profiles II and III are the consecutive flattening of Profile I. Profile IV is based on the empirical fit obtained for Crow and Champagne's data and is the closest to what has been observed in experiments. Profile IV has a thinner initial shear layer that is naturally unstable. We therefore

expect Profile IV to be the most unstable among those studied, and the present calculations indicate that this is indeed so. It was found during our calculations that the flatter profiles (Profiles III, IV) became numerically unstable when the jet Reynolds number was increased. This is basically due to the lack of proper grid resolution, which is necessary for higher Reynolds number calculations. Therefore, to make proper comparisons and to keep the solutions time-accurate, the solutions presented here are all in the Reynolds number range from 200 to 300.

Figures 19a through 19d give the steady-state vorticity contours for the four velocity profiles (I through IV), respectively. [In all the following figures, unless otherwise stated, the y-z plane refers to the plane $x = x_j$, while the x-z plane refers to the plane $y = y_j$ (see Figure 1).] For direct comparison, the contour intervals are the same in all the figures. The Reynolds numbers are not the same for all the cases but are close enough to make comparison possible. Except for Profile IV, all solutions are at nearly the same elapsed time. Comparing the vorticity for different profiles shows that the vortex zone above the ground plane is much larger for Profile IV as compared to the other profiles. The vorticity levels also increase from Profile I to the much flatter profile (Profile IV). Near the ground plane there is an indication of a pinching effect on the vorticity line above the vortex zone in all the x-vorticity plots. This is perhaps because as the flow spreads on the ground plane, a part of the flow gets entrained into the jet region, thereby causing the vortex lines to get pushed towards the centerline.

In the wall boundary layer, a region of secondary vortical circulation opposite to the large primary vortex appears, as can be seen in the x-vorticity contours (Figure 19). Note here that solid lines indicate vorticity out of the plane and dashed lines indicate vorticity into the plane. This region of secondary vorticity also moves downstream along with the primary vortex. This formation of secondary vorticity in the wall boundary layer has been associated with boundary layer separation (Didden and Ho, 1985), and the present calculations seem to predict qualitatively their experimental observation. In Didden and Ho's experiments, they observed the secondary vorticity lifting off the plate and wrapping itself around the primary vortex. They also observed the breakup of the large primary ring vortex as the flow continues to spread on the ground and attributed this to possible azimuthal instability. This has not been observed in the present calculations, however, due to the proximity of the outflow boundary to the jet. With a larger computational domain and better resolution near the ground, it may be possible to study these experimental observations. The general picture is qualitatively the same for all the different profiles studied here and is consistent with general experimental observations. However, direct comparison is not possible due to the low-Reynolds-number simulations carried out here and also due to the possible effect of the type of boundary conditions employed. Higher resolution simulations on a large computational domain (in the x- and y-directions) and at higher Reynolds numbers are necessary for detailed comparisons with the available experimental data.

The appearance of the secondary vorticity of the opposite sign on the ground plane is observed for all the velocity profiles studied here. To get a better look at this secondary vorticity in the wall boundary layer, in

Figure 19e we show for comparison a higher resolution (24x48x24) calculation with the ground plane at H/D = 1 and at a Reynolds number of 600. For this calculation we assumed symmetry in both the x- and y-directions and, therefore, only the half-planes were calculated. The propagation of the primary vortex in the downstream direction is evident in this figure, and the formation of the secondary vorticity of the opposite sign is also very clear. Moreover, the initial attempt by the secondary vorticity to wrap itself around the primary vortex as they move downstream is also shown, consistent with the experimental observation (Didden and Ho, 1985). However, this process is affected by the outflow boundary location, and the wrapping process seems to be inhibited.

To determine details of the pressure variation, we show the variation of the pressure along the centerline in Figure 20a. The pressure values are normalized by the maximum value at the stagnation point, and the centerline location is also normalized by the distance between the jet exit and the ground plane. The variations for both Profiles I and III are quantitatively the same and, for comparison, some experimental data (Beltaos and Rajaratnam, 1973; Russell and Hatton, 1972) for the centerline pressure variation are also presented. We found that most of the experimental data available are for two-dimensional or axisymmetric high-Reynolds-number turbulent flows and, therefore, good agreement is not expected since the present calculations are for low-Reynolds-number, three-dimensional laminar flow. The variation of the calculated pressure is similar to that seen in experiments and indicates that the present calculations are predicting qualitatively the observed pressure distribution.

To determine the possible existence of an adverse pressure gradient, we plotted the variation of the wall pressure (normalized by the stagnation pressure) for both Profiles I and III, as a function of radial (x) direction, in Figure 20b. The pressure decreases from the maximum at the stagnation point until $x/H \simeq 0.085$ (for Profile III) and $x/H \simeq 0.1$ (for Profile I), at which point it starts to increase again indicating a change from a favorable to an adverse pressure gradient. We could conclude based on this figure that there is a possible occurrence of separation at $x/D = 0.80$ (for Profile I) and $x/D = 0.68$ (for Profile III). However, this separation effect is possibly due to the collision of the wall jets on each other and the formation of the fountain. Also shown in Figure 20b are the available experimental data for the high-Reynolds-number turbulent impinging jets, which indicate similar variation. The appearance of an adverse pressure gradient on the ground plane is interesting since it has been experimentally identified as the cause of unsteady separation of the wall shear layer. Additional data is required to confirm whether there is any separation occurring on the ground plane. For example, the pressure variation in the y-direction and the variation of the wall shear stress must be calculated to determine the location where it changes sign, which would then indicate the separation point. The grid resolution near the ground would also have to be improved to resolve the wall boundary layer. These factors will be considered in more detail in the future study.

Figure 20c gives the variation of the steady-state centerline velocity (normalized by the maximum velocity at the jet exit and the distance of the jet from the ground plane) as a function of distance to the ground plane for

169

Profiles I and III. Also shown are some characteristic experimental data for high-Reynolds-number turbulent impinging jets. Though direct comparison is not possible, the general trend in the present calculation is similar to that of the experimental data. The solution also indicates that the decay along the centerline is much slower for Profile III than for Profile I. This is probably due to the fact that Profile III, with its flatter profile shape, has a more distinct potential core as compared to Profile I, which is parabolic, with hardly any potential core. Since in potential core there is (by definition) no dissipation, the velocity decay occurs slower and hence closer to the ground plane for a Profile III-type jet as compared to a Profile I-type jet.

In general, the steady-state solutions presented above for impinging jets indicate qualitative agreement with experimental data. Four different initial jet profiles were studied, and the comparison indicates that the flatter profiles show more signs of instability. Furthermore, it was found that the flatter profiles showed numerical instability for higher-Reynolds-number simulations and, therefore, all the present calculations were carried out in the Reynolds number range from 200 to 300. This numerical instability is mainly due to the lack of adequate resolution in the computational domain and, due to the computer resource restrictions, the largest mesh used is (16x32x64). For quantitative comparison with experimental data and more detailed interpretation of the complex flow structures observed here, a higher resolution (and higher Re) simulation is envisioned in the future study.

The overall flow pattern indicates that the initial shear layer rollup is not observed due to lack of resolution near the jet exit. However, the formation of the large primary vortex ring is observed, and when this vortex ring impinges on the ground plane and spreads in the radial direction, the formation of secondary vorticity of the opposite sign in the wall boundary layer is also observed. This secondary vorticity in the wall layer may be due to separation, since the pressure data indicate the presence of an adverse pressure gradient near the outflow (in the x-direction). However, this is not exactly the same effect as observed by Didden and Ho (1980) due to the effect of the fountain in the present study. Comparison with experimental data for high-Reynolds-number turbulent impinging jets indicates qualitative agreement for the centerline and ground plane pressure variation and the centerline velocity variation.

3.2 Single-Frequency Forcing

3.2.1 Axisymmetric Forcing

The study of turbulent shear flows has undergone considerable change in the recent past, brought about by the discovery of large, spatially coherent structures in fully developed flows. Furthermore, it has been realized that the initial instability of the flow can have a strong influence on its subsequent evolution. For example, Crow and Champagne (1971) observed that growth and mixing of an axisymmetric jet were sensitive to harmonic forcing and found a "preferred" frequency for the development of the jet for a Strouhal number, $St(= fD/U)$, of 0.3. They also observed that, as the Reynolds number was increased from 10^2 to 10^3, the instability of the jet evolved from a sinusoidal to a helical mode and finally into a train of axisymmetric waves. It

has also been noted that the initial jet exit velocity profile plays an important part in determining the form of instability that is observed. A top-hat profile has been shown to be more unstable than a fully developed profile (Batchelor and Gill, 1962; Grant, 1974) due to the shear layer instability. In some experiments, the instability of the initial shear layer occurs through axisymmetric modes, whereas in other experiments a helical instability was observed first (Strange and Crighton, 1983; Hussain, 1983). Such differences are attributed, in part, to the initial conditions of the experimental setup. Therefore, to study the stability of jet flows, the initial instability mechanism must be understood. Moreover, since it has been shown that large eddies in jet flows can be controlled by harmonic forcing, the effect of controlled forcing on the instability mechanism is also important.

In the present numerical study of an impinging turbulent jet, the mesh resolution is limited by the available computer storage. It is, therefore, not possible to study the effect of a wide band turbulence, i.e., a wide range of disturbances in frequency and wave numbers. However, it is possible to look at the unsteady behavior of the jet flow due to forcing at a specific frequency of disturbance. We have done some preliminary forcing studies, whereby the initial jet exit velocity is perturbed at a given frequency of oscillation. An attempt has been made to determine the characteristic (or preferred) frequency for a given jet profile, and this frequency has been used to impose unsteadiness at the jet exit. We expect that, if the frequency of disturbance corresponds to the most unstable mode, some form of axisymmetric instability will be observed.

To further understand the effect of the initial instability, we have studied its effects on different velocity profiles, for example, Profiles I, II, and III. Moreover, since the helical mode of instability has also been experimentally observed, we have done some preliminary calculations by introducing at the jet exit an unsteady disturbance that has azimuthal variations. By imposing a disturbance in space (azimuthal) and time at the jet exit, we have attempted to force the shear layer similar to the experimental conditions. If the frequency of the disturbance corresponds to the most unstable mode, then the shear layer should roll up in a manner similar to the experiments. For both free and impinging jets (as in V/STOL flows), the most unstable frequency (due to shear layer instability) is probably the same since this type of instability is a function of the shear layer thickness at the jet exit, and the ground effect is negligible there. However, the jet preferred mode type of instability (based on jet diameter), which appears in the later stage of jet development, will probably be affected by the location of the ground plane due to possible pressure feedback and resonance effects. When the ground plane is far from the jet exit, this instability mechanism should correspond to that for a free jet. Some characteristic results are presented for the single-frequency forcing at $St = 0.3$ for the computational domain used in the steady-state calculations [(Equation (2)]. The forcing was begun after the flow field had reached steady state. Some studies were also carried out for the case when the forcing was initiated before the flow field reached steady state, or before the large primary vortex ring reached the ground plane, to determine the effect of initial transients on the instability mechanism and its effects on the primary vortex development.

For these single-frequency studies the jet exit velocity was perturbed such that

$$w_j = \bar{w}_j[1 + \varepsilon(t)] \tag{4}$$

where $\bar{w}_j$ is the original jet profile given by Equation (3) and $\varepsilon(t)$ is a sinusoidal pulse defined by a frequency, ω and an amplitude, A. At present, the frequency used in all the axisymmetric forcing studies corresponded to a Strouhal number, St = 0.3. The amplitude of the forcing was varied from 10 to 30 percent of the mean velocity. These forcing levels were relatively high as compared to experimental forcing studies (Crow and Champagne, 1971). However, numerical simulation with lower forcing levels would require more forcing cycles (partly due to the low Reynolds number) and hence more computer time, which was not available. Therefore, it was decided to study qualitatively rather than quantitatively the effect of forcing on the jet. It must be pointed out here that available literature indicates that numerical simulation of forced three-dimensional free or impinging jets has not been studied in detail and, therefore, these preliminary calculations are directed toward determining a possible future direction in the study of excited free and impinging jets. We intend to carry out more detailed and higher resolution forcing studies in the future that are tailored to make direct comparisons with experimental studies possible.

Figures 21a through 21e give the vorticity contours for a jet of Profile I at Re = 200 and forced at St = 0.3 with a 30-percent amplitude level plotted every $\pi/2$ intervals of a forcing cycle. The forcing was begun after the flow field had reached steady state, and the data shown are for the fourth cycle of forcing. All vorticity contour intervals are maintained the same to facilitate comparison. Periodic shedding of the large vortex ring is clearly evident in these figures. As the ring vortex approaches the ground, the vorticity spreads and the ring vortex loses its identity. The spreading of the vorticity also causes a bulge in the vortex lines as it approaches the ground. As the primary vortex moves down the jet, a new vortex ring appears there, which also subsequently is shed. Comparing Figures 21a and 21b, which show the vorticity contours at the beginning and the end of the fourth forcing cycle, we see that the solution essentially repeats itself. Hence, we can conclude that the period of vortex shedding is essentially the same as the period of forcing.

If we measure the distance between two successive primary vortex cores, we obtain a wavelength $\lambda/D \simeq 2.1$. This compares reasonably well with Didden and Ho's (1985) wavelength of $\lambda/D \simeq 1.7$. For St = 0.3, the frequency of the present forcing study is also 0.3 (since, here, D = U = 1). Then the convection velocity of the vortex ring is $U_c = \lambda f = 0.63$ U. The experimental data of Didden and Ho (1985) indicate $U_c = 0.61$ U, which indicates that the present simulation can predict reasonably the global behavior of forced impinging jets.

Comparing the y-vorticity component at different times, we see that the vortex has a tendency to elongate as it approaches the ground plane, where it finally merges into the originally steady ground vortex. The formation of secondary vorticity of the opposite sign in the wall layer is also observed in these figures. It is possible that, during these forcing studies, the wall boundary layer undergoes unsteady separation as was observed by Didden and Ho

172

(1985). In viscous flows, the wall acts as a vorticity source, and when the ring vortex impinges on the ground and starts to spread in the radial (x,y)-direction, it induces a shear layer on the wall where a secondary region of opposite vorticity appears. As shown by Didden and Ho (1985), this secondary vortex region can exist prior to separation and, therefore, separation is not the reason for the appearance of the secondary vorticity. However, due to the external forcing, the wall shear layer is also unsteady and may possibly separate, and secondary vorticity is always associated with separation. Lack of resolution near the wall made it difficult to determine the point of separation (if any) in these unsteady calculations. For comparison, we show in Figures 22a through 22d, the vorticity contours for the forced case of Profile III under the same conditions as for Profile I. In general, the vorticity pattern is similar though the levels are much higher and more details of the ring vortices are evident.

A similar forcing study was done with the flow at different stages of its initial development with a view to determining the effect of controlled forcing on the transient development of an impinging jet. This has some relevance to V/STOL-type flow fields, since in reality the steady-state situation is never achieved and instability waves are probably excited during the transient development. In general, the forcing study with initially unsteady flow indicates that the primary vortex ring is shed periodically as before, with the shedding repeating itself each period. This indicates that the unsteadiness in the flow field does not significantly affect the flow region close to the jet exit partly due to the fact that the effect of forcing is much stronger near the exit. However, there is a clear indication that the consequent development of the primary ring vortex and its interaction with the ground plane does not repeat itself. There is also some indication of vortex stretching and tearing near the ground. The region of secondary vorticity continues to increase as a function of time, and the initial ring vortex near the ground decreases in size and seems to stay fixed at its initial impact position.

To obtain an idea of how the vorticity field looks in three dimensions, we present a series of figures in Figure 23 in which we show the three-dimensional perspective view of the total absolute vorticity, $|\omega| = \sum_{i=1}^{3} |\omega_i|$, where i=1,3 indicates the three coordinates. The vertical axis is in the z-direction, and the x-y plane is shown at the bottom. Since we assumed symmetry in the x-direction, only the half-plane is shown. These perspective plots show the three-dimensional absolute vorticity surface at a given time. The level in the figure indicates the value of the $|\omega|$ surface shown, such that all values of $|\omega|$ greater than the given level are contained within the three-dimensional $|\omega|$ surface. These levels were chosen such that 12 percent of the volume of the computational domain is contained within the three-dimensional surface. If the level of vorticity is increased, the higher values of vorticity that would be shown would be contained in a smaller volume. The 12-percent value was chosen since it gave the best overall perspective of the vorticity surface in three dimensions. These plots do not show the vorticity direction, since only the absolute value of the vorticity is shown.

Figure 23a gives the three-dimensional vorticity surface for steady state of Profile I at Re = 200. The primary vortex structure above the ground can be clearly seen. Also observable is the secondary vorticity imprint on the

ground plane. The space between the two vortex tube-like structures in the jet does not imply that there is no vorticity present there. Instead, what it means is that the vorticity level there is lower than the level shown. Figure 23b gives the three-dimensional vorticity surface in 12-percent volume for the case of forcing at St = 0.3 of Profile I flow. This figure shows the characteristic bulges due to the primary vortex shedding and also indicates that the vorticity level shown does not remain similar to the steady-state case shown in Figure 23a. Figure 23c shows the steady-state vorticity surface (again in 12-percent volume) for Profile III at Re = 200. The vorticity levels are higher, indicating that in the same volume as in Figures 23a and 23b, more vorticity is present. The structure of the ground plane vortex is also quite different. Forcing this steady-state solution at St = 0.3 shows a more distinct pattern of vortex shedding as can be seen in Figure 23d, which is the forced vorticity surface for Profile III.

Three-dimensional perspective plots, such as those shown in Figure 23, can be used to get an idea of the complicated three-dimensionality of the flow field and the associated structures in the flow. It cannot, however, be used to obtain a detailed picture of the actual flow (as shown in the vorticity contours before) since the final details are usually smeared and hidden inside the vorticity surface such as that shown in Figure 23.

3.2.2 Axisymmetric Forcing with Crossflow

The numerical code developed so far is capable of investigating additional flow phenomena relevant for VTOL-type flow fields. Examples of such flows are impinging jets in a crossflow, which models the forward motion of a VTOL aircraft close to the ground, and inclined impinging jets, which models a VTOL aircraft in a climb mode. We have carried out some preliminary forcing studies for such complex phenomena. For these simulations we used an 18x72x18 mesh in a computational domain defined by

$$-1 \leq x/D \leq 1$$
$$-2 \leq y/D \leq 2 \qquad (5)$$
$$0 \leq z/D \leq 1$$

such that the ground plane is very close to the jet exit. We therefore expect the presence of the ground to have an effect on the flow field generated.

In the following, we discuss the effect of unsteady forcing at the jet exit in the presence of crossflow. The grid mesh used in these calculations was 18x72x18 with symmetry in the x-direction. These simulations were carried out with forcing at St = 0.3 and a crossflow of 40 percent of the mean velocity. The amplitude of the forcing was also 40 percent of the mean value. Simulation with 20-percent forcing amplitude was also carried out, and the results were qualitatively the same, though the higher amplitude forcing case showed the features of the flow field more clearly and is presented here. The results presented in the following figures are at equal time intervals and therefore do not correspond to any one complete cycle of the forcing. However, they show some interesting flow phenomena that merits presentation.

Figure 24a gives the velocity distribution in the y-z plane as a function of time. The solution indicates the periodic formation of a clockwise vortex near the ground. This vortex is a direct consequence of unsteady separation of the wall shear layer. This is due to the adverse pressure gradient that periodically occurs on the ground plane. Examining the pressure gradient for the corresponding times (not shown here) indicated that there is high pressure ahead of the vortex zone and lower pressure behind the vortex zone, resulting in separation of the wall shear layer and lift off from the ground, which results in the vortex formation. The vortex disappears when the pressure gradient periodically changes from adverse to favorable. Though the solutions presented in these calculations are not for any complete forcing cycle, the results do indicate that the vortex forms due to the periodic variation in the jet velocity. This results in periodic formation of the adverse pressure gradient near the wall, causing the wall shear layer to undergo unsteady separation and form the vortex zone.

Figure 24b gives the corresponding velocity distribution in the x-z plane at $y = y_d$ (see Figure 1) for the same times. The flow field shows that the large primary vortex zone completely dominates the region above the ground plane. This is due to the proximity of the ground to the jet exit. The flow patterns also indicate the periodic formation of a "kidney"-shaped vortex region. Note that this kidney-shaped vortex zone is not the same as the one observed in jets with crossflow (Andreopoulos and Rodi, 1984).

Figures 25a and b gives the corresponding vorticity in the two center-planes. The shedding of the primary vortex is clearly evident. However, the vortex ring is no longer symmetric and is compressed on the side that faces the crossflow, as can be seen in the y-z plane. The vorticity pattern is much more complex, with the primary vortex ring distorted by the effect of cross-flow. The secondary vorticity region is clearly evident in both the y-z and the x-z planes. However, the region of secondary vorticity also periodically moves, indicating that the location of the separation point is also a function of the periodic formation of the vortex zone. The secondary vorticity zone also shows periodic attempts to wrap itself around the primary vortex core (x-z plane), but does not seem to complete itself, perhaps due to the proximity of the downstream boundary.

In conclusion, single-frequency axisymmetric forcing studies at St = 0.3 have been carried out for various initial jet profiles. The solutions indicate good qualitative agreement with experimental observations of impinging jets. The flatter profiles (Profiles III and IV) show more signs of instability as compared to Profile I. The primary vortex shedding frequency corresponds very closely to the forcing frequency. These forcing studies show that the axisymmetric instability mode can be excited, but additional forcing simulations need to be carried out to determine the most unstable frequency (for jet preferred instability), since a range of 0.2 < St < 0.5 has been observed to be unstable experimentally. Also, it is not clear at present what the presence of the ground plane has on the instability mechanism in terms of modification of the unstable frequency. Due to lack of resolution, the most unstable frequency for the shear layer instability was not observed. This frequency would correspond to St $\simeq$ 0.017 (based on the shear layer momentum thickness). But forcing studies at this frequency have not been carried out at present because of the lack of resolution to observe the shear layer rollup. However, the forcing at

the jet preferred mode (for St = 0.3) showed a periodic shedding of axisymmetric vortex rings. The calculations also indicate the formation of secondary vorticity in the wall shear layer of the opposite sign consistent with experimental observation (Didden and Ho, 1985). This region of secondary vorticity may be due to separation of the wall shear layer, and there are some indications that this is indeed so. The presence of the adverse pressure gradient on the ground plane is probably due to the collisions of the wall jets at the base of the fountain. There is some indication of unsteady separation on the ground plane. This unsteady separation phenomenon seems to be a consequence of external forcing and indicates that the forcing technique can be used to study the separation phenomena, which is of great interest and is a region not well understood. More detailed calculations with a higher resolution grid are necessary before any further conclusions can be made.

Our forcing study of the impinging jet in a crossflow indicates that there is an unsteady formation of a ground vortex, again probably due to the change in the pressure field (due to forcing), resulting in unsteady separation of the wall shear layer and the consequent rollup of the wall shear layer.

The effect of the ground plane on the forcing seems to be minimal when the ground plane is far from the jet exit. More research is necessary, however, to determine how the ground plane location would modify the instability mechanism. It is clear that the jet shear layer instability mode (not observed here) would not be affected by the ground plane, though the jet preferred mode would probably be affected by the wall due to possible feedback from the wall resulting in pressure resonance effects. The present calculations are for incompressible flows and, therefore, there is no acoustic field (noise) generation during the impingement process. There could, however, be effects of the variation of the hydrodynamic pressure in the region between the jet and the impinging wall, which could result in some modification of the impinging jet stability mechanism. This is due to the fact that for impinging jets there are three modes of instability: the jet shear layer instability (based on the shear layer thickness), the jet preferred mode (based on the jet diameter), and the resonance mode (based on the location of the ground plane). All three modes of instability can be excited and are very important in the study of impinging jets. At present, only the jet preferred mode has been studied in these simulations, and additional parametric studies are necessary to determine the interaction between the three modes of instability. This is an area of research that will be considered in more detail in the future study.

3.2.3 Single-Frequency Forcing with Azimuthal Variation

Forcing studies were also carried out to determine whether the helical mode of instability can also be excited. For this purpose the jet was forced at a given frequency with an azimuthal variation. The forcing function is assumed to be of the form

$$w_j(x, y, t) = \overline{w_j}(x, y) [1 + \varepsilon_H(x, y, t)] \tag{6}$$

where the forcing function $\varepsilon_H(x, y, t)$ is defined as

$$\varepsilon_H(x, y, t) = A \sin(n\omega t + k\theta) \tag{7}$$

where ω is the forcing frequency and $n = 1, 2, \ldots$ gives the various modes. Also, A is the forcing amplitude and $\theta \; [= \tan^{-1}(y/x)]$ is the azimuthal variation with k as the wave number. The solutions presented here are for $n = k = 1$, which corresponds to the fundamental mode excitation with an azimuthal variation. Results for some preliminary calculations were recently presented (Rizk and Menon, 1985). These results indicate that the helical instability mode can be excited by forcing with azimuthal variation. The initial forcing simulations were carried out with a coarse (14x17x32) mesh at a low Reynolds number of 100. The ground plane was located at H/D = 5 and, therefore, the initial jet development is close to that for a free jet. The Strouhal number corresponding to the frequency of forcing was varied (0.08 < St < 0.5) to determine the effect of the frequency on the excitation of the instability. The results shows that the effect of forcing on the jet development is significant, even in these low-Reynolds-number and coarse-grid calculations. In these preliminary study, the excitation was begun before the jet reached the ground plane and, therefore, the instability was excited during the unsteady development of the jet. Characteristic vorticity contours for helical forcing at St = 0.165 is presented in Figure 26 which showed some sort of alternate vortex shedding. There seems to be an indication that a flapping mode of instability has been observed, but due to the fact that these studies were with a coarse mesh, the details of the instability are not clear.

To study the helical instability mechanism in even more detail, a series of forcing simulations for St = 0.3, 0.46, 0.67 was carried out using the higher resolution grid (16x32x64) and the computational domain given by Equation (2). The general pattern of instability was observed to be similar, and here we show the characteristic results for the forcing case with St = 0.3. In this calculation, the forcing amplitude was 30 percent of the mean, and the forcing was initiated after the flow field had nearly reached steady state. Due to computer resource limitations, it was decided not to take the solution out to complete steady state at present. Figure 27 gives the vorticity contours in the two planes for forcing at St = 0.3 plotted every $\pi/2$ of the seventh period of forcing. Note here again that no symmetry assumptions have been made and the whole computational domain given by Equation (2) has been calculated. The jet is therefore located in the center of the top surface. Since these figures represent a complete cycle of forcing, we can follow the development and the convective motion of the vortex rings. As can be clearly seen in these figures, the vorticity is shed alternately at the jet exit, and there is no sign of the axisymmetric mode of the instability. There is also an indication that the vortex core may be undergoing some sort of pairing. The period of vortex shedding is the same as the period of forcing, as can be seen by comparing the figures for the beginning and the end of the period. As pointed out by Hussain (1983), it is possible that what is observed may not be the helical instability but rather tilting of the axisymmetric ring vortex due to the azimuthal variation of the flow velocity. It is clear that the form of instability observed during forcing with azimuthal variation is quite different from that observed during the axisymmetric forcing studies.

In conclusion, detailed calculations with a relatively fine mesh have been carried out to study the effect of both axisymmetric and helical forcing of a low-Reynolds-number impinging jet. Only a single-frequency forcing study has been carried out in detail. The results indicate the characteristic shedding of the vortex rings as a function of forcing frequency during axisymmetric forcing, and the twisting and alternate shedding (or tilting) of vorticity is observed for helical forcing. Pressure variation along the ground plane shows the appearance of an adverse pressure gradient in the x-z plane, which is probably due to the fountain effect in the outflow boundary. A region of secondary vorticity is present in the ground plane, which is consistent with experimental observation (Didden and Ho, 1985). Due to lack of resolution and data (in the y-z plane) in the wall region, it was not possible to determine conclusively whether there was any unsteady separation in the wall layer during the forcing, which has been experimentally observed. The present calculations indicate that the numerical simulations carried out here for both steady-state and forcing cases showed qualitative agreement with experimental observations. However, there are many aspects of the study that warrant improvement and that will be considered in the future research. For example, the grid resolution and the Reynolds number will be increased for a more realistic simulation by using subgrid-scale modeling and grid refinement. Additional forcing studies to determine the effect of the ground plane on the instability development will also be carried out. More realistic turbulence simulations will be carried out by imposing a random turbulence field at the jet exit. Grid resolution near the jet exit will be refined to observe the shear layer rollup. Additional data in the ground plane will be sampled to determine whether there is any unsteady separation occurring in the wall shear layer during forcing.

3477R

References

Agarwal, R. K., and Bower, W. W. (1982) "Navier-Stokes Computations of Turbulent Compressible Two-Dimensional Impinging Jet Flowfields," _AIAA J._, Vol. 20, May, pp. 577-584.

Andreopoulos, J., and Rodi, W. (1984) "Experimental Investigation of Jets in a Crossflow," _J. Fluid Mech._, Vol. 138, pp. 93-127.

Batchelor, G. K., and Gill, A. E. (1962) "Analysis of the Stability of Axisymmetric Jets," _J. Fluid Mech._, Vol. 14, pp. 529-551.

Beltaos, S. and Rajaratnam, N. (1973), "Plane Turbulent Impinging Jets," _J. Hydraul. Res._, Vol. 11, No. 1, pp. 29-59.

Bower, W. W., Agarwal, R. K., Peters, G. R., and Kotansky, D. R. (1979) "Viscous Flowfields Induced by Two- and Three-Dimensional Lift Jets in Ground Effect," Report ONR-CR215-246-3F, March.

Buzbee, B. L., Golub, G. H. and Nielson, C. W. (1970) "On Direct Methods for Solving Poisson's Equations," _SIAM J. Numer. Anal._, Vol. 7, December, pp. 627-656.

Childs, R. E. and Nixon, D. (1985) "Simulation of Impinging Turbulent Jets," AIAA Paper 85-0047, January.

Crow, S. C. and Champagne, F. H. (1971) "Orderly Structure in Jet Turbulence," _J. Fluid Mech._, Vol. 48, August, pp. 547-591.

Didden, N. and Ho, C.-M. (1985) "Unsteady Separation in a Boundary Layer Produced by an Impinging Jet," To Appear in _J. Fluid Mech._

Grant, A. J. (1974) "A Numerical Model of Instability in Axisymmetric Jets," _J. Fluid Mech._, Vol. 66, Part 4, pp. 707-724.

Harlow, F. H., and Welch, J. E. (1965) "Numerical Calculation of Time-Dependent Viscous Incompressible Flow of Fluid with Free Surface," _Phys. Fluids_, Vol. 8, pp. 2182-2189.

Hussain, A. K. M. F. (1983) "Coherent Structures - Reality and Myths," _Phys. Fluids_, 26, pp. 2816-2850.

Hussain, A. K. M. F. and Zaman, K. B. M. Q. (1981) "The 'Preferred Mode' of the Axisymmetric Jet," _J. Fluid Mech._, 110, pp. 39-71.

Kotansky, D. R. and Bower, W. W. (1978) "A Basic Study of the V/STOL Ground Effect Problem for Planar Flow," _J. Aircraft_, Vol. 15, April, pp. 214-221.

Moin, P. and Kim, J. (1982) "Numerical Investigation of Turbulent Channel Flow," _J. Fluid Mech._, Vol. 118, May, pp. 341-377.

179

Rizk, M. H., and Menon, S. (1985) "A Numerical Investigation of VTOL Aero-dynamics," Communication No. 170, Research and Technology Division, Flow Industries.

Rubel, A. (1978) "Computations of Jet Impingement on a Flat Surface," AIAA Paper 78-207, January.

Rubel, A. (1981) "Computations of the Oblique Impingement of Round Jets Upon a Plane Wall," AIAA J. Vol. 19, July, pp. 863-871.

Russell, P. J., and Hatton, A. P. (1972) "Turbulent Flow Characteristics of an Impinging Jet," Proc. of Institute of Mech. Engineers, Vol. 186, pp. 635-644.

Strange, P. J. R. and Crighton, D. G. (1983) "Spinning Modes on Axisymmetric Jets, Part 1," J. Fluid Mech., Vol. 134, September, pp. 231-245.
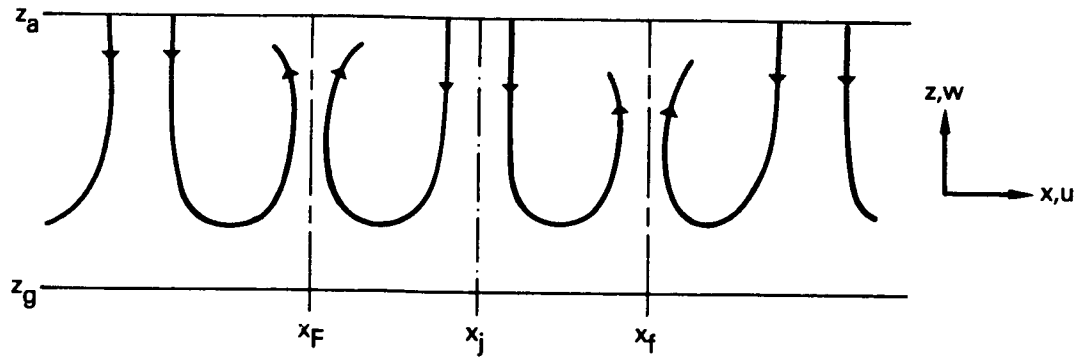
SIDE VIEW
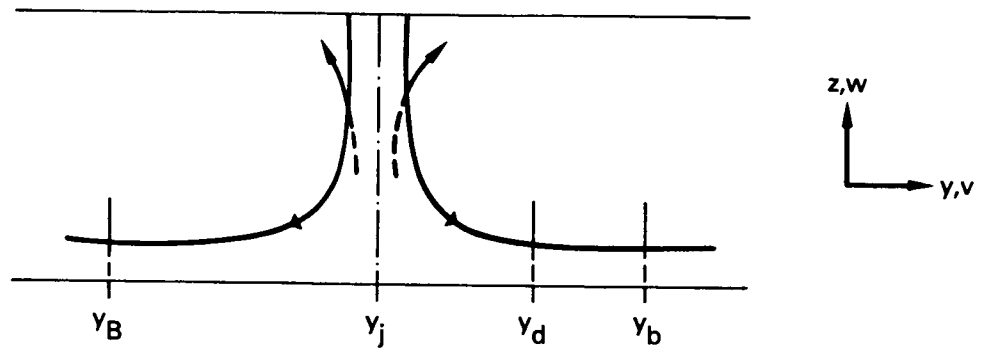
END VIEW

Figure 1.   Model Problem for a Hovering VTOL Aircraft
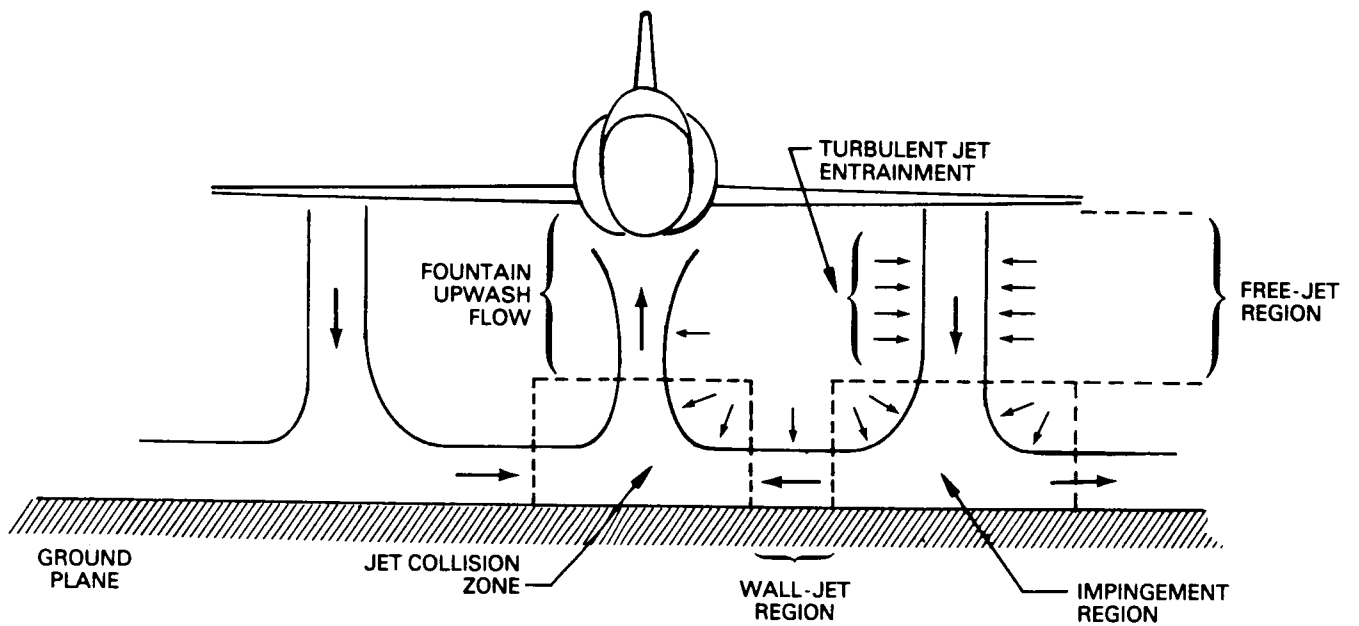
Figure 2.   Schematic of Flow Field About a Hovering VTOL Aircraft
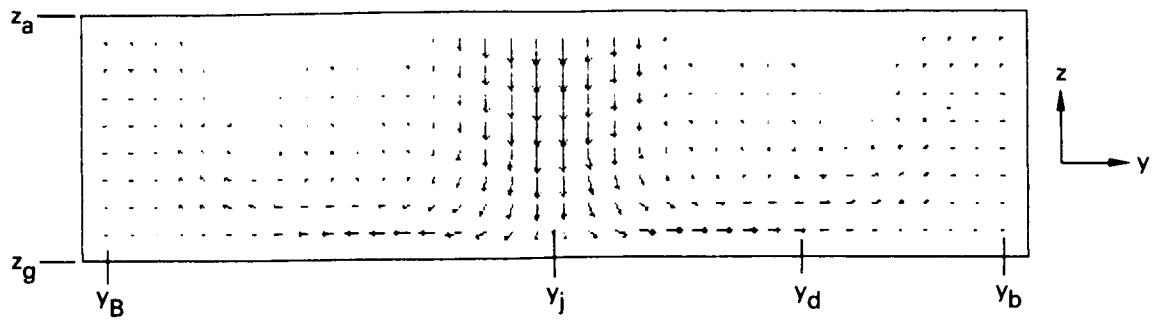
Figure 3. Example 1: Velocity Vectors in the Plane x = x_j
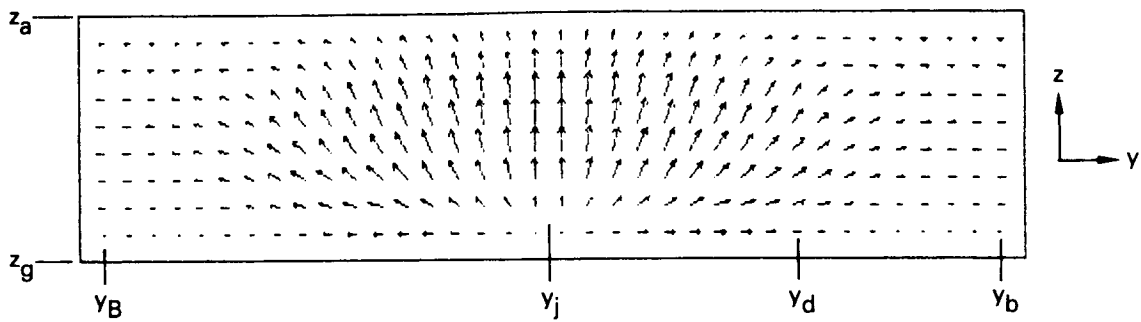
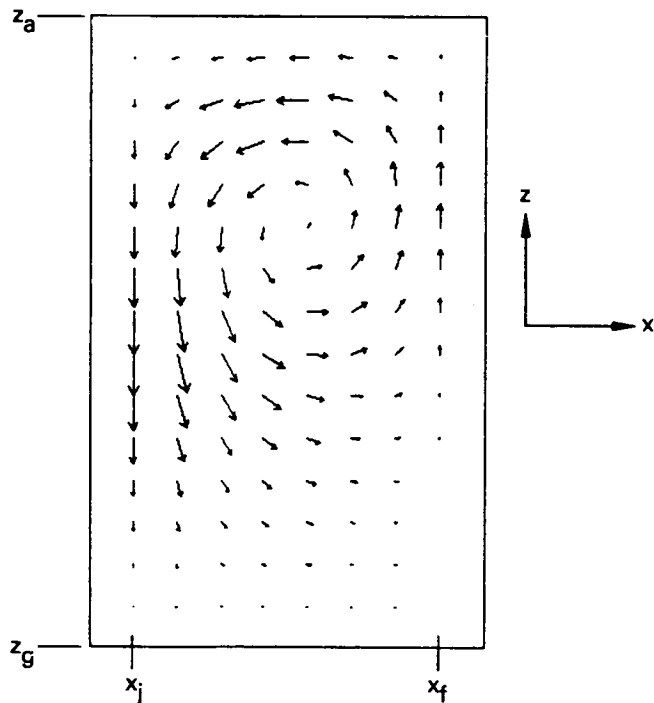**Figure 4. Example 1: Velocity Vectors in the Plane x = x_f**
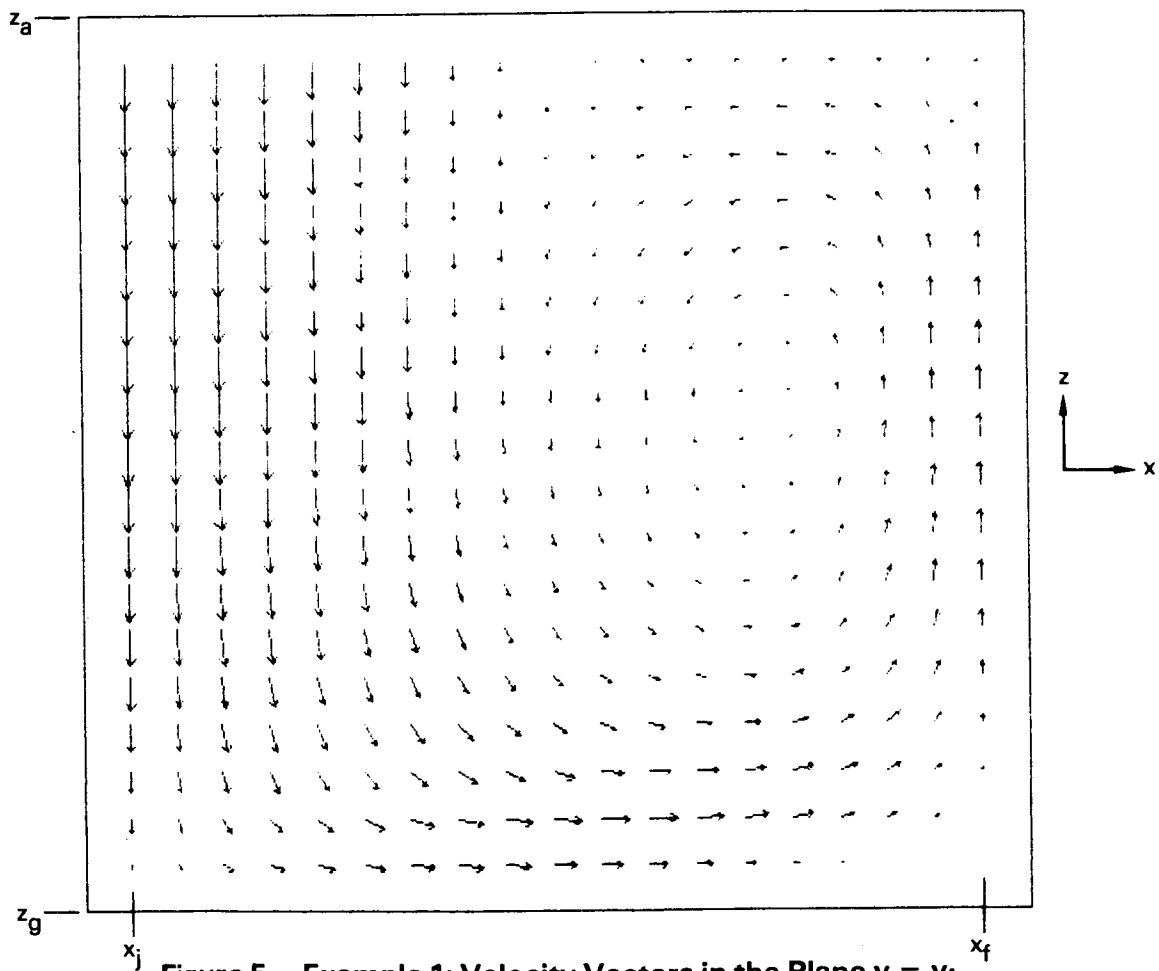
Figure 5. Example 1: Velocity Vectors in the Plane y = y_j
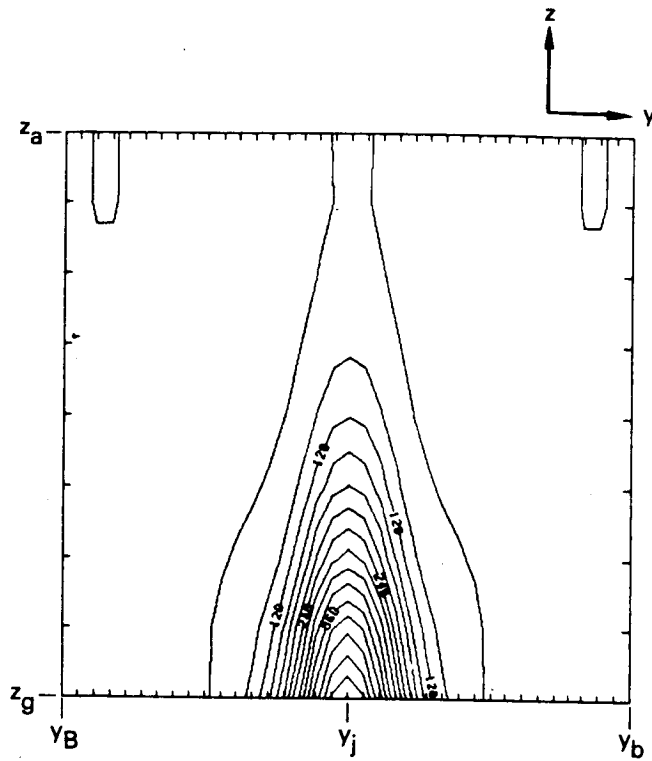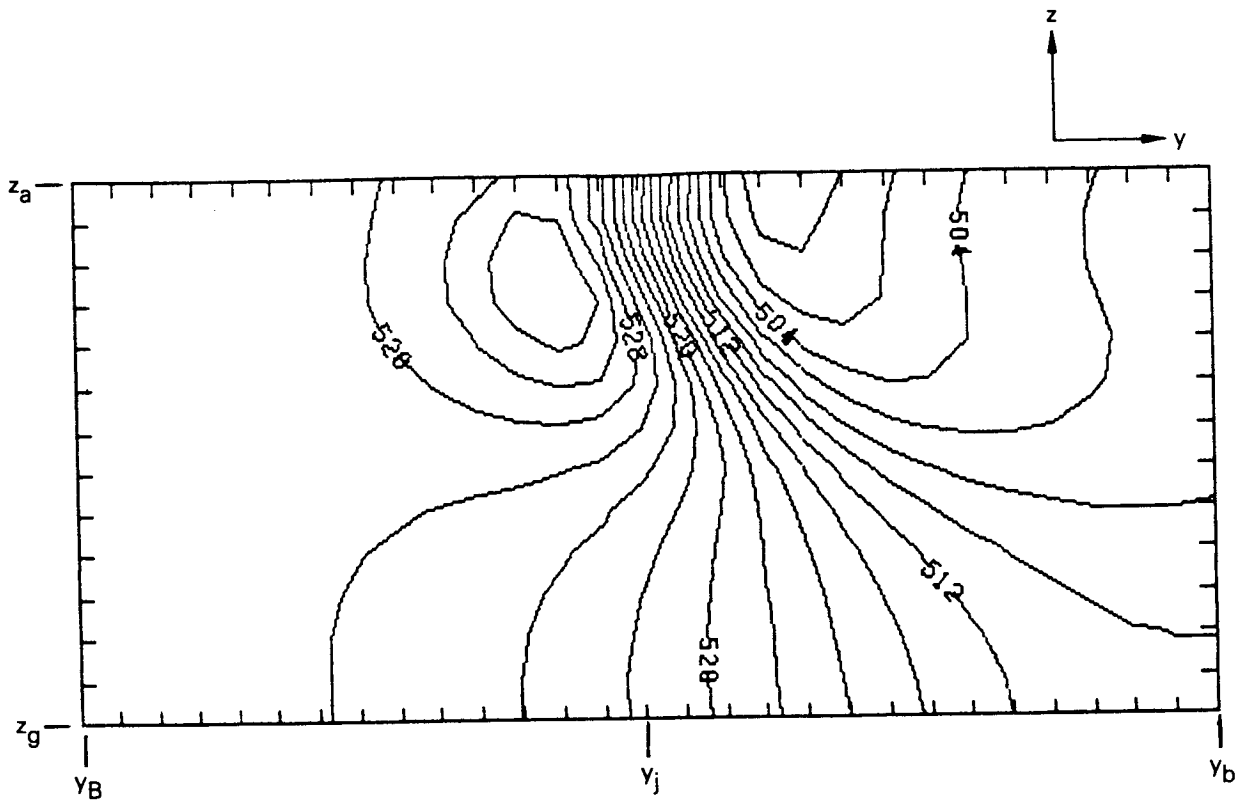
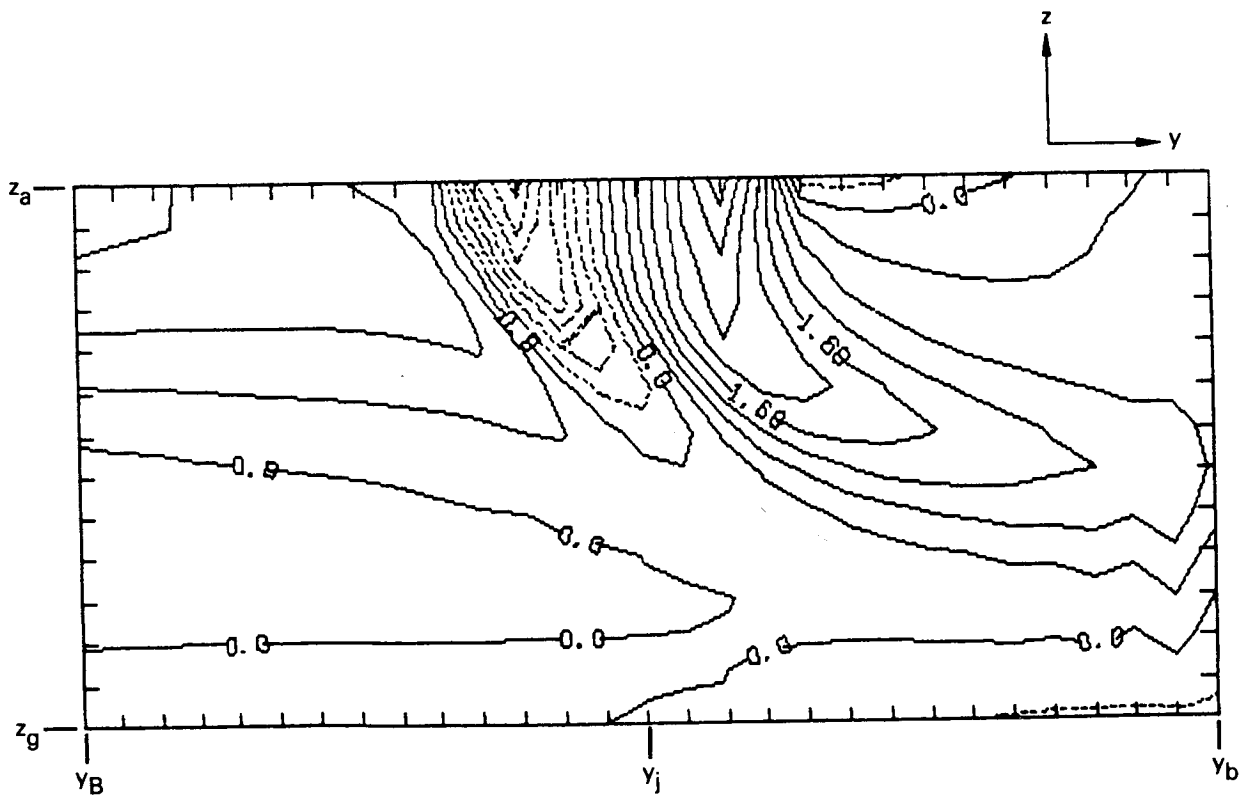Figure 6. Example 1: Pressure Contours in the Plane x = x_j
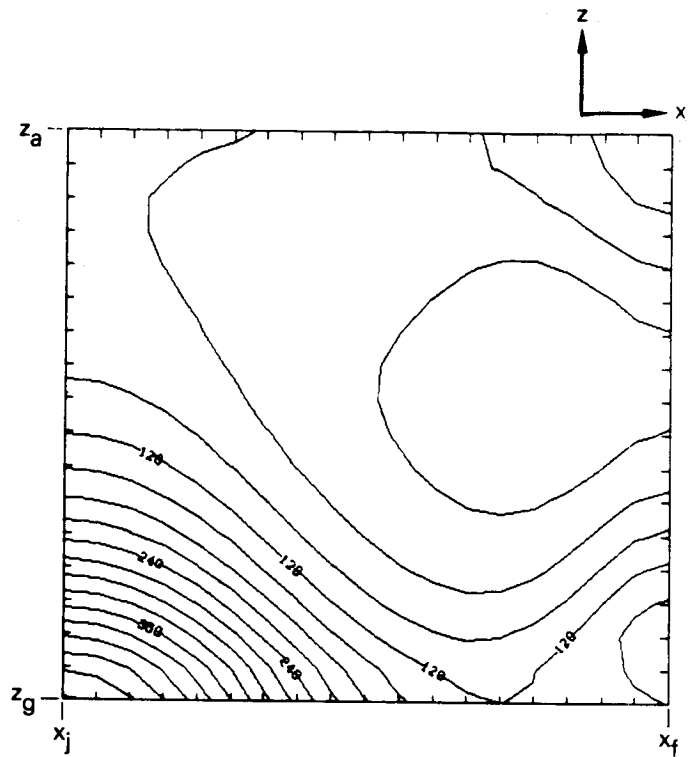
Figure 7. Example 1: Pressure Contours in the Plane y = y_j
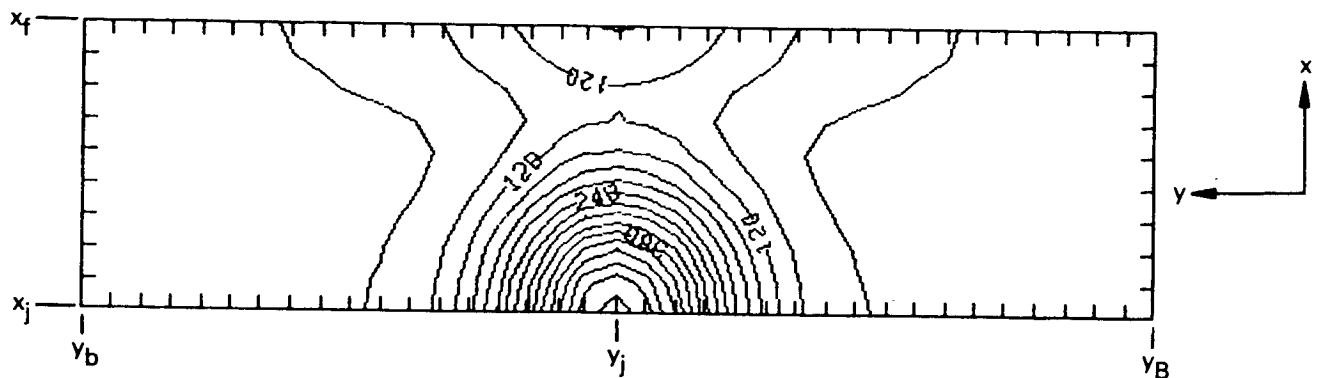
Figure 8. Example: Pressure Contours in the Plane z = z_g
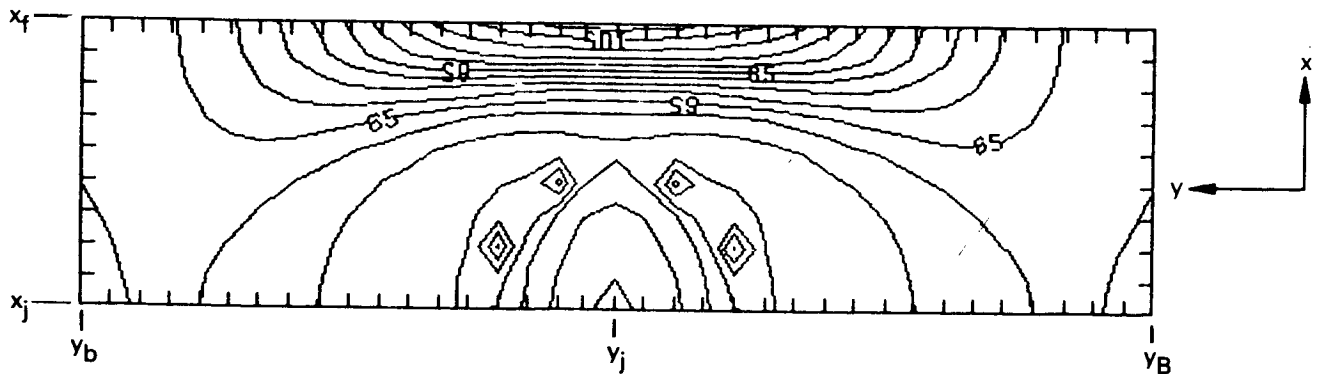
Figure 9. Example 1: Pressure Contours in the Plane z = z_a

183
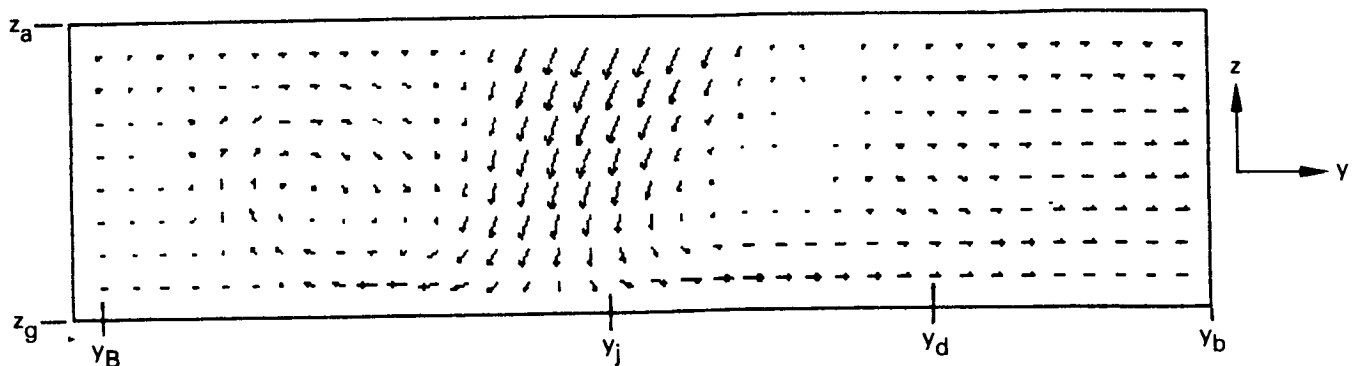
Figure 10.   Example 2: Velocity Vectors in the Plane x = x$_j$
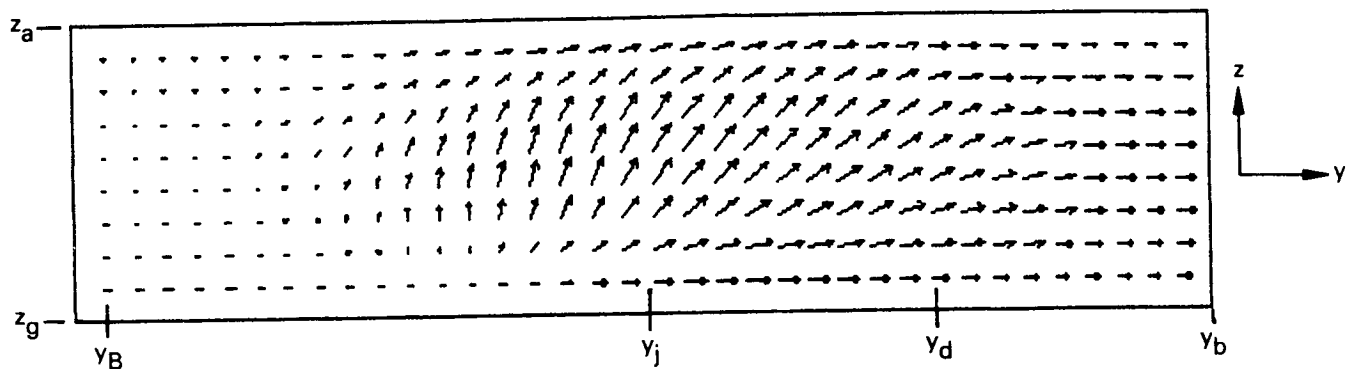
Figure 11.   Example 2: Velocity Vectors in the Plane x = x$_f$
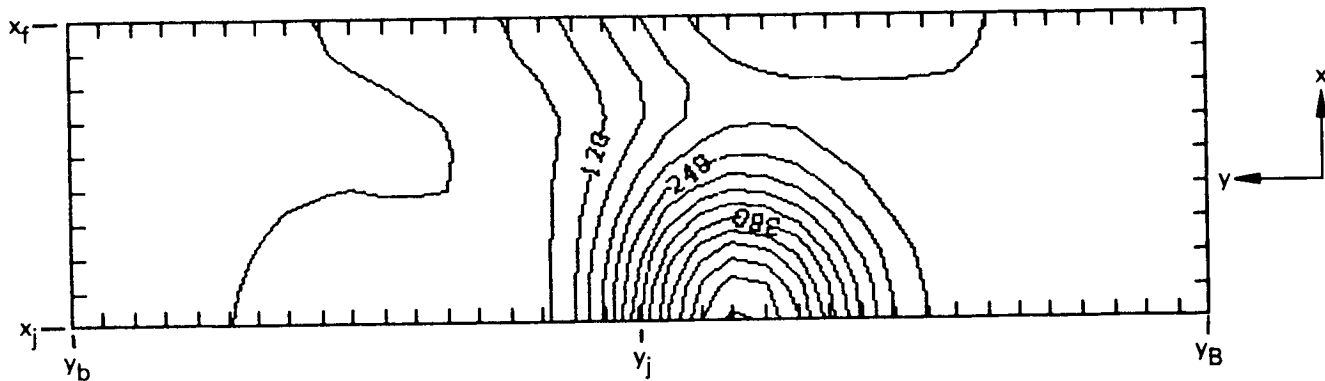
Figure 12.   Example 2: Pressure Contours in the Plane z = z$_g$
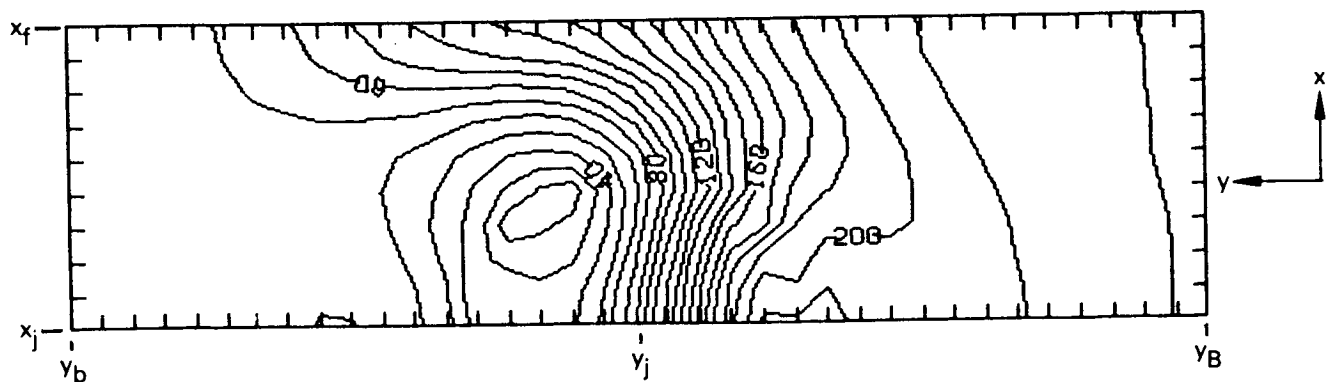
Figure 13.   Example 2: Pressure Contours in the Plane z = z$_a$

184
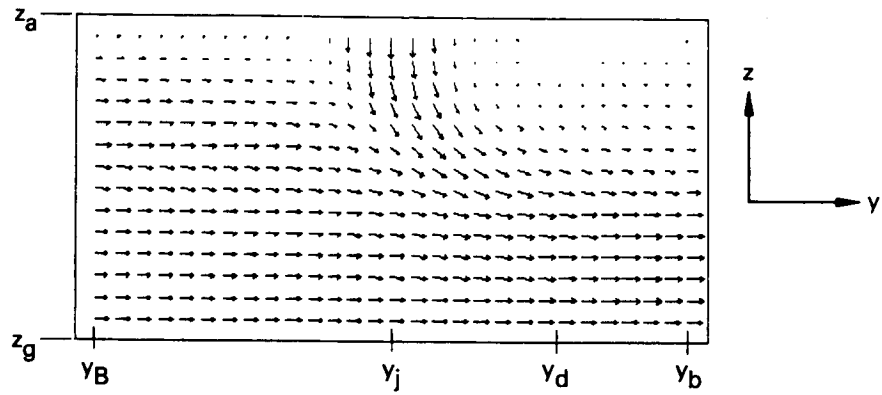
Figure 14. Example 3: Velocity Vectors in the Plane x = x$_j$
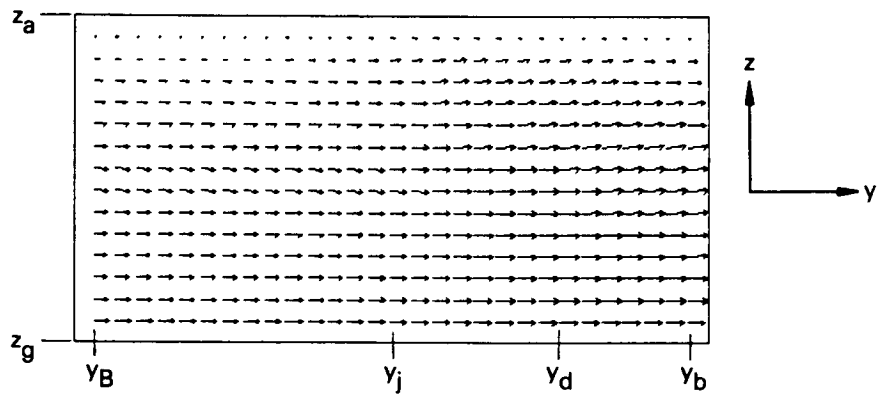
Figure 15. Example 3: Velocity Vectors in the Plane x = x$_f$

Figure 16. Example 3: Velocity Vectors in the Plane y = y$_d$

Figure 17.   Example 3: Pressure Contours in the Plane x = x$_j$

Figure 18.   Example 3: x-Vorticity Component in the Plane x = x$_j$

186

C - 3

X - Vorticity Component, Y-Z Plane, x = x_j

Y - Vorticity Component, X-Z Plane, y = y_j

a. I Re = 200
       T = 45.94

b. II Re = 250
       T = 43.75

c. III Re = 200
        T = 45.94

d. IV Re = 300
        T = 32.8

e. Primary Vortex Propagation on the Ground for Profile I, Re = 600, Mesh = 24 × 48 × 24
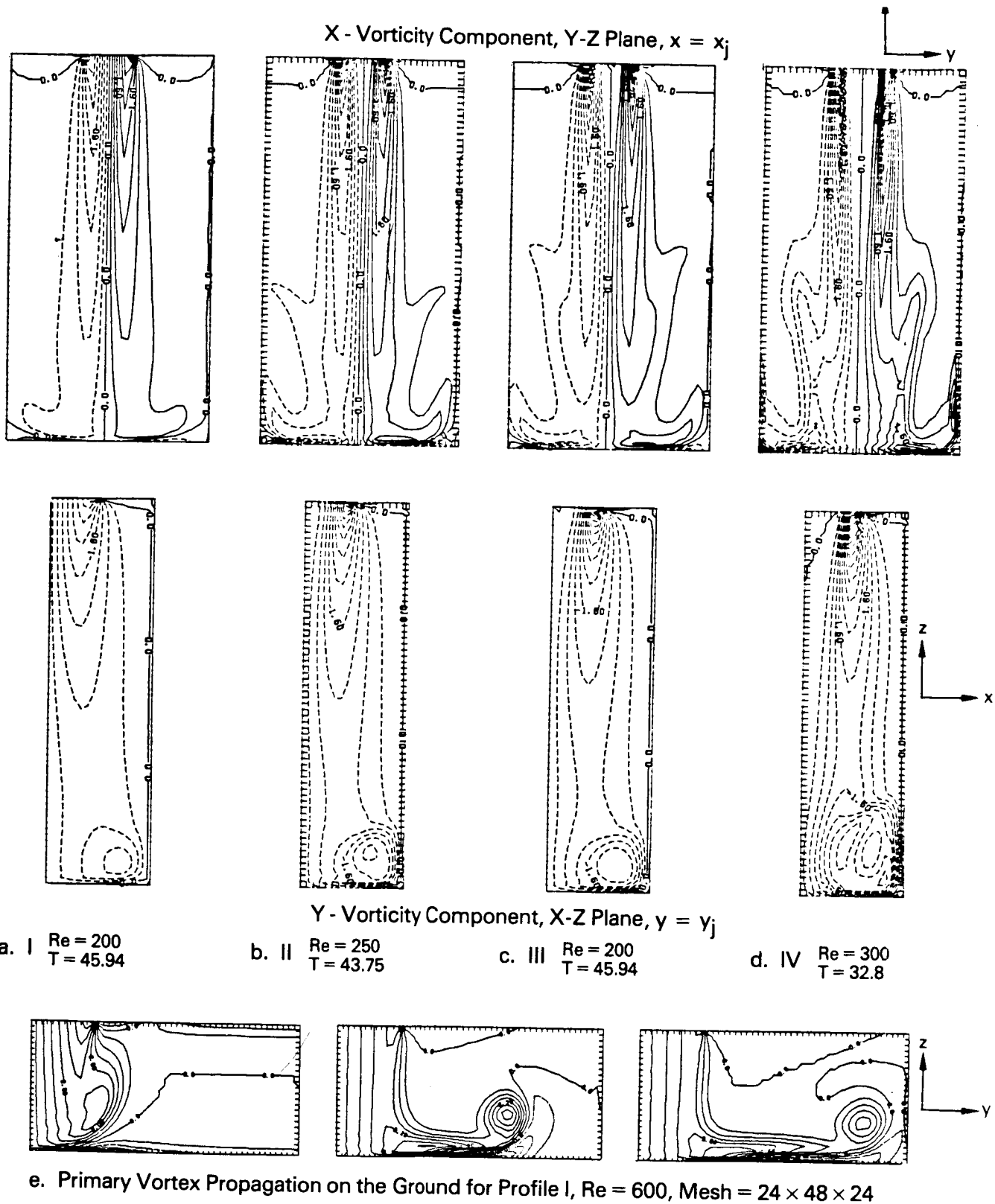
Figure 19.   Steady State Vorticity Contours for Profiles I - IV
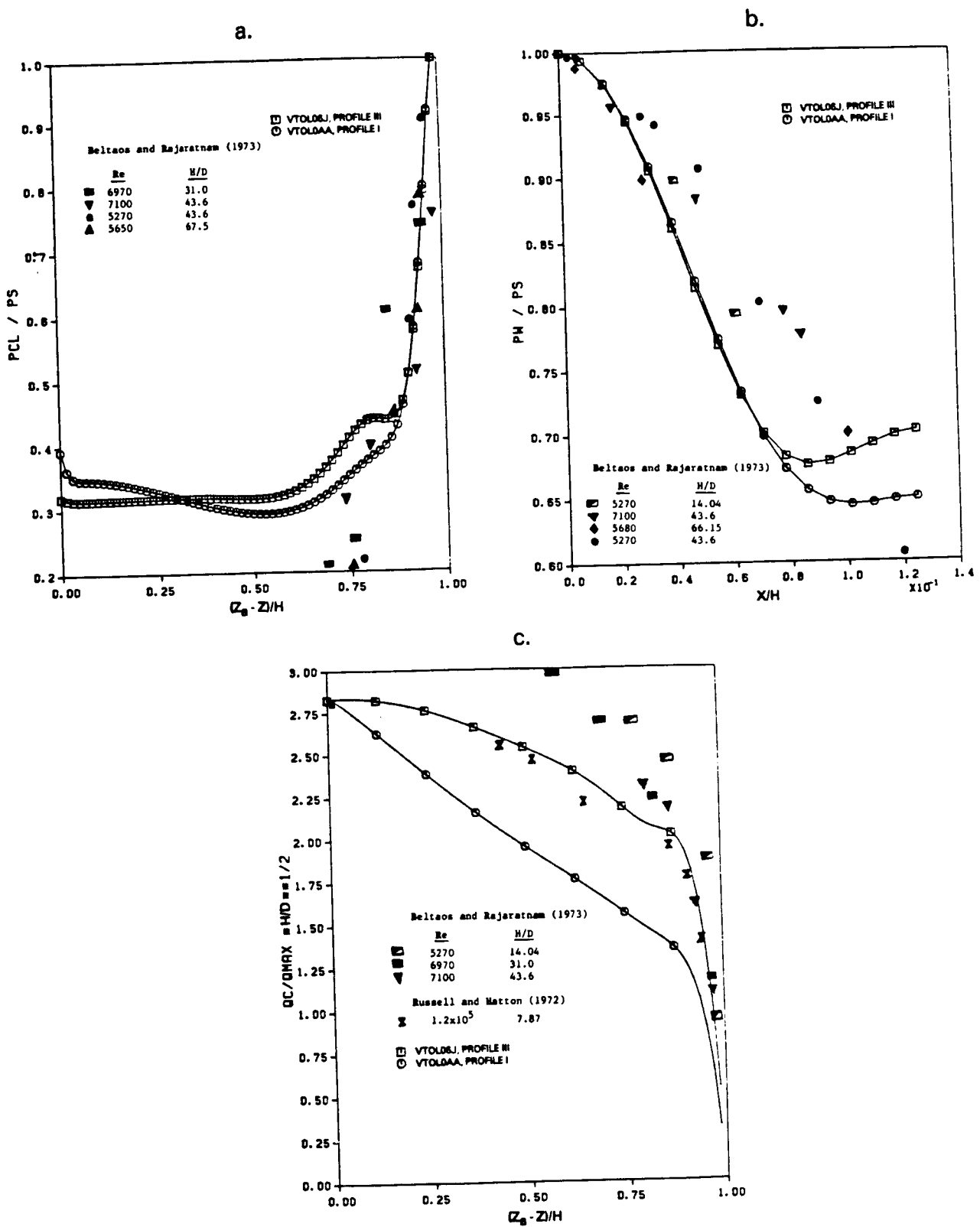
Figure 20. a. Steady State Pressure Variation Along Centerline. Re = 200, T = 45.94

b. Steady State Ground Plane Pressure Variation in X-Z Plane. Re = 200, T = 45.94

c. Steady State Centerline Velocity Variation. Re = 200, T = 45.94

X - Vorticity Component, Y-Z Plane, x = x_j
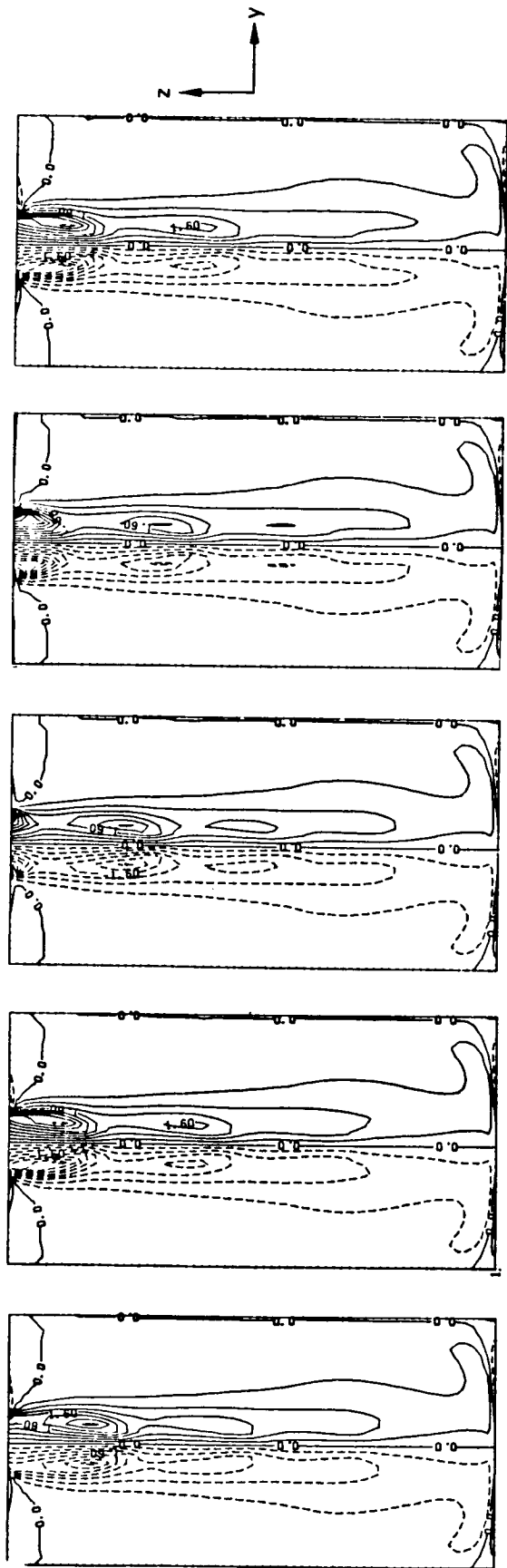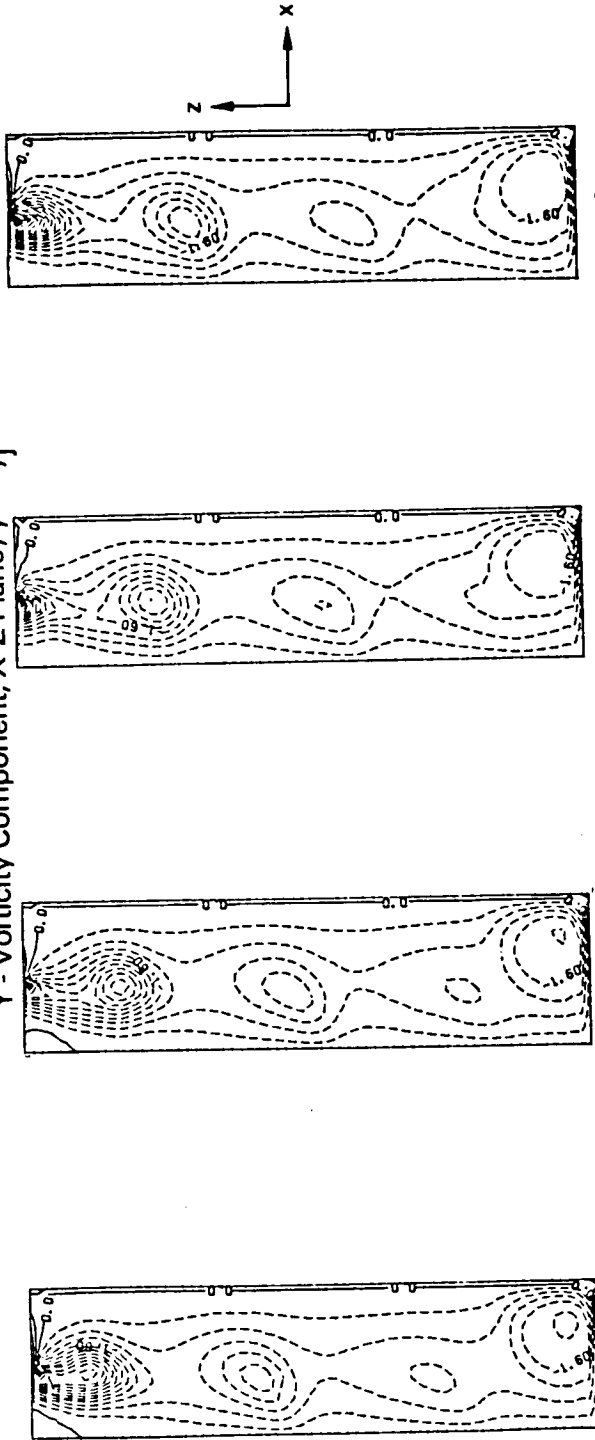
Y - Vorticity Component, X-Z Plane, y = y_j
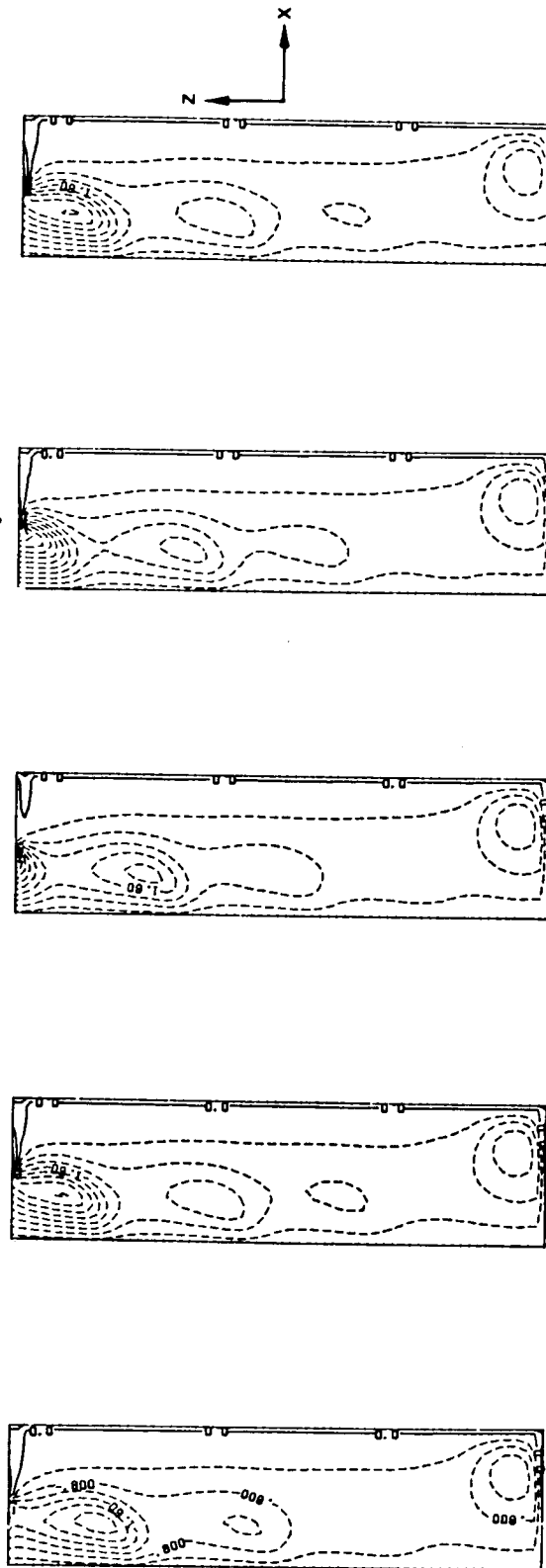
a. T = 55.8, θ = 0

b. T = 56.59, $\theta = \pi/2$

c. T = 57.42, $\theta = \pi$

d. T = 58.25, $\theta = 3\pi/2$

e. T = 59.06, $\theta = 2\pi$

Figure 21. Vorticity Contours for Profile I at Re = 200 and Forced Axisymmetrically at St = 0.3. Plots are Every $\pi/2$ of the Fourth Period

189

X - Vorticity Component, Y-Z Plane, x = x_j
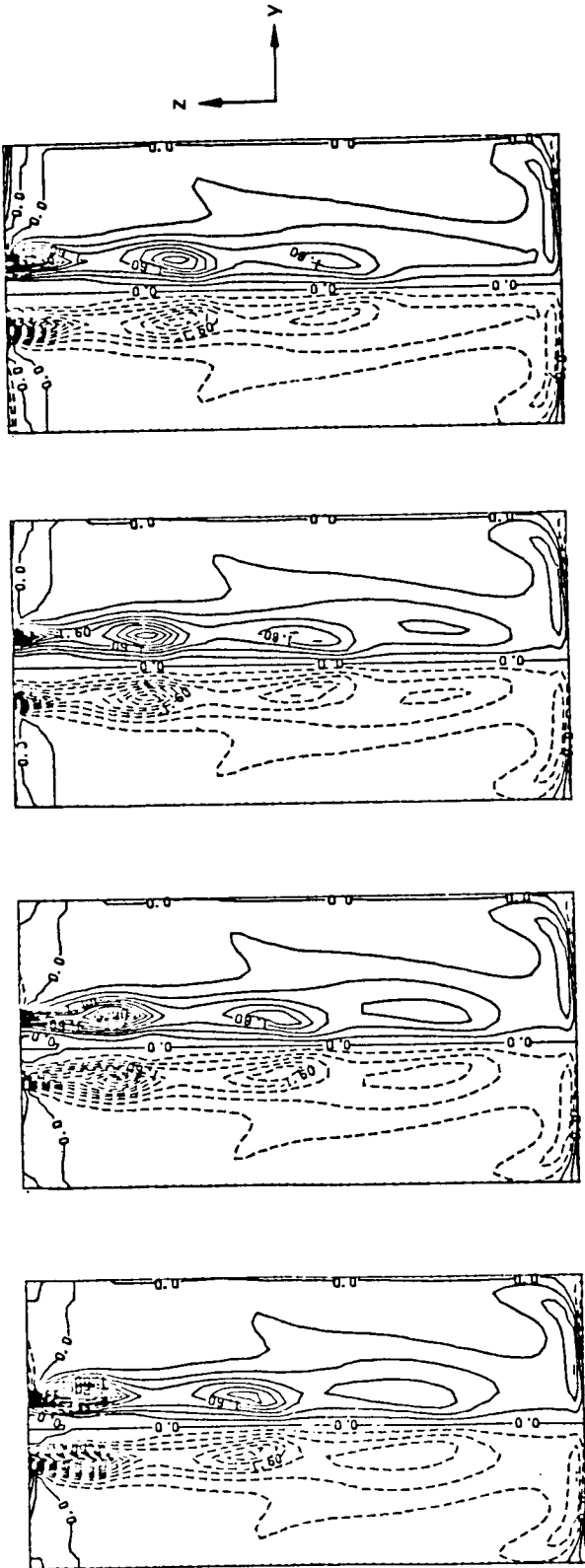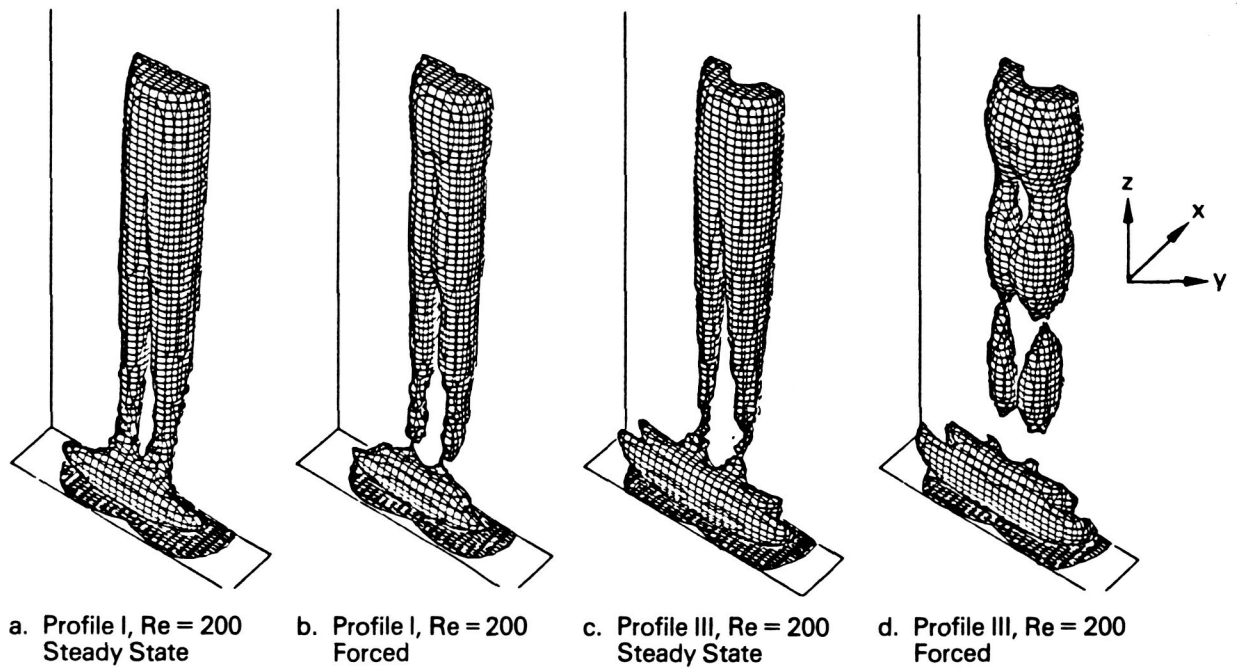
Y - Vorticity Component, X-Z Plane, y = y_j

a. T = 49.24, θ = 0

b. T = 50.03, θ = π/2

c. T = 50.86, θ = π

d. T = 51.7, θ = 3π/2

Figure 22. Vorticity Contours for Profile III at Re = 200 and Forced Axisymmetrically at St = 0.3. Plots are Every π/2 of the Fourth Period

190

a. Profile I, Re = 200
   Steady State

b. Profile I, Re = 200
   Forced

c. Profile III, Re = 200
   Steady State

d. Profile III, Re = 200
   Forced

Figure 23.   Perspective Plot of the Absolute Total Vorticity Surface in Three Dimensions

T = 15.56

T = 17.5

T = 19.44

T = 21.4

a. Y-Z Plane, $x = x_j$

T = 15.56

T = 17.5

T = 19.44

T = 21.4

b. X-Z Plane, $y = y_d$
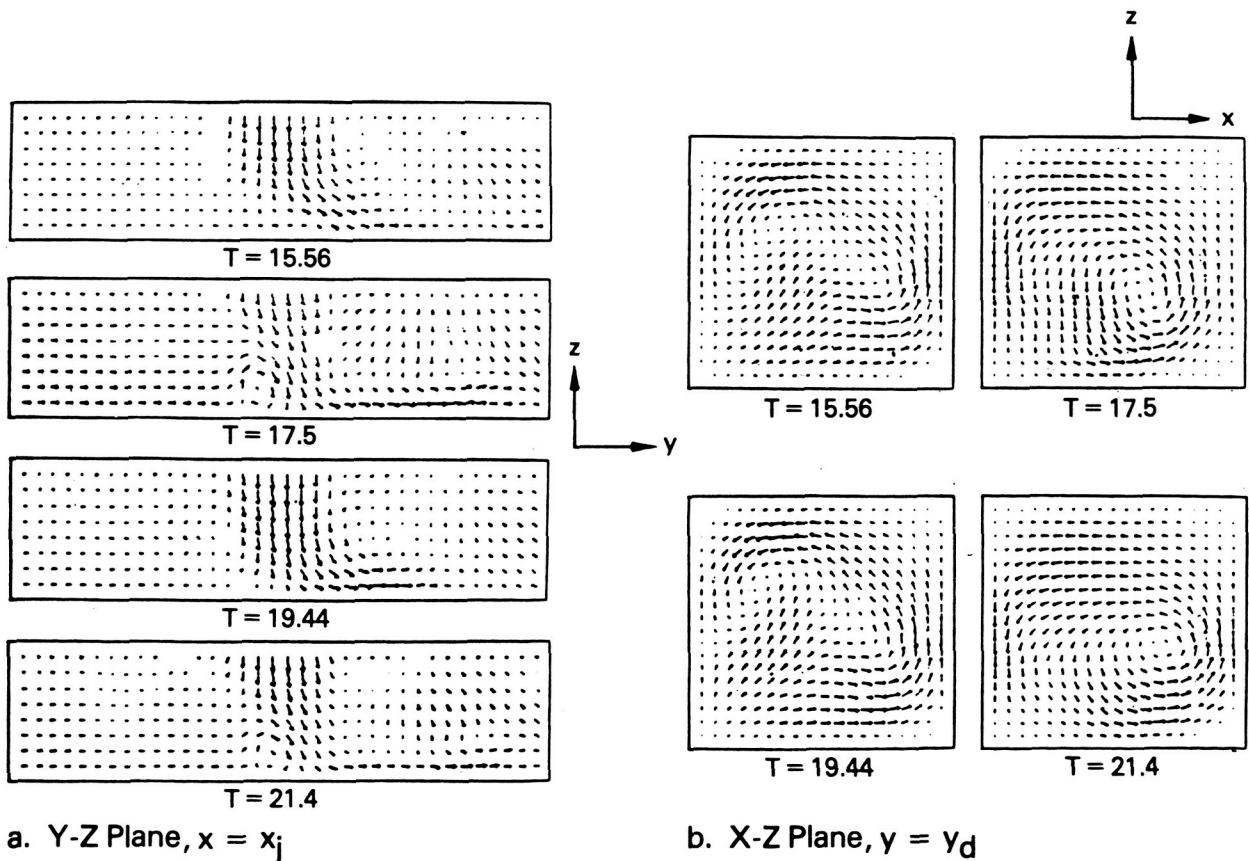
Figure 24.   Velocity Distribution for Profile I at Re = 300 with 40% Crossflow and Forced Axisymmetrically at St = 0.3

X - Vorticity Component, Y-Z Plane , x = x_j

T = 15.56   T = 17.5   T = 19.44   T = 21.4
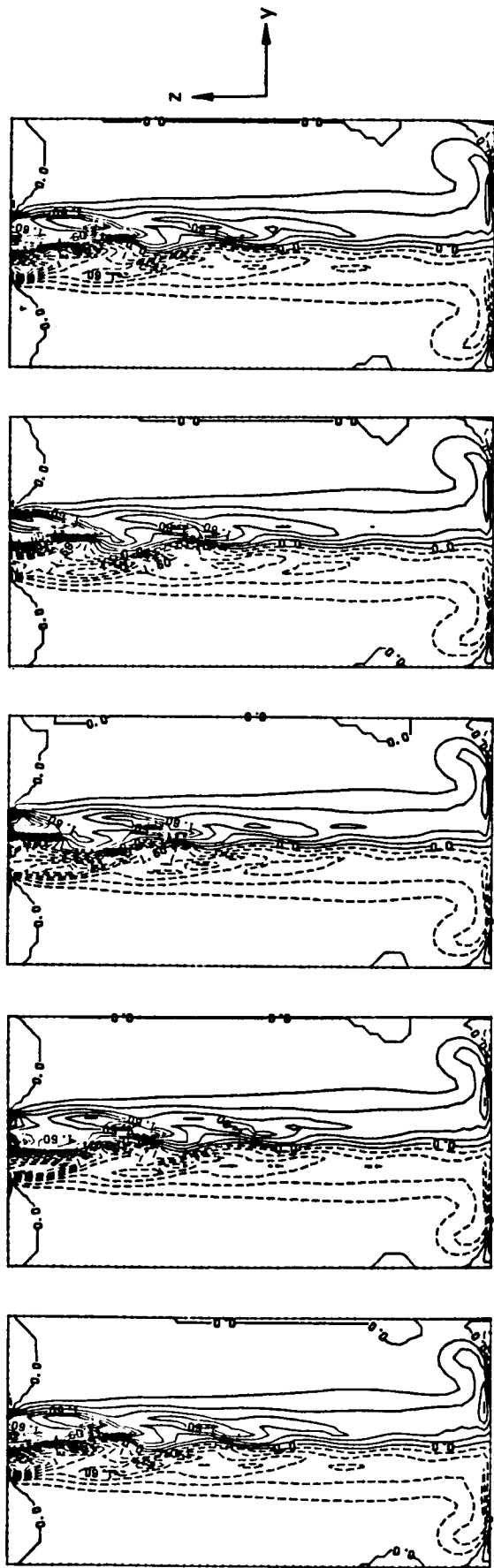
Y - Vorticity Component, X-Z Plane, y = y_j
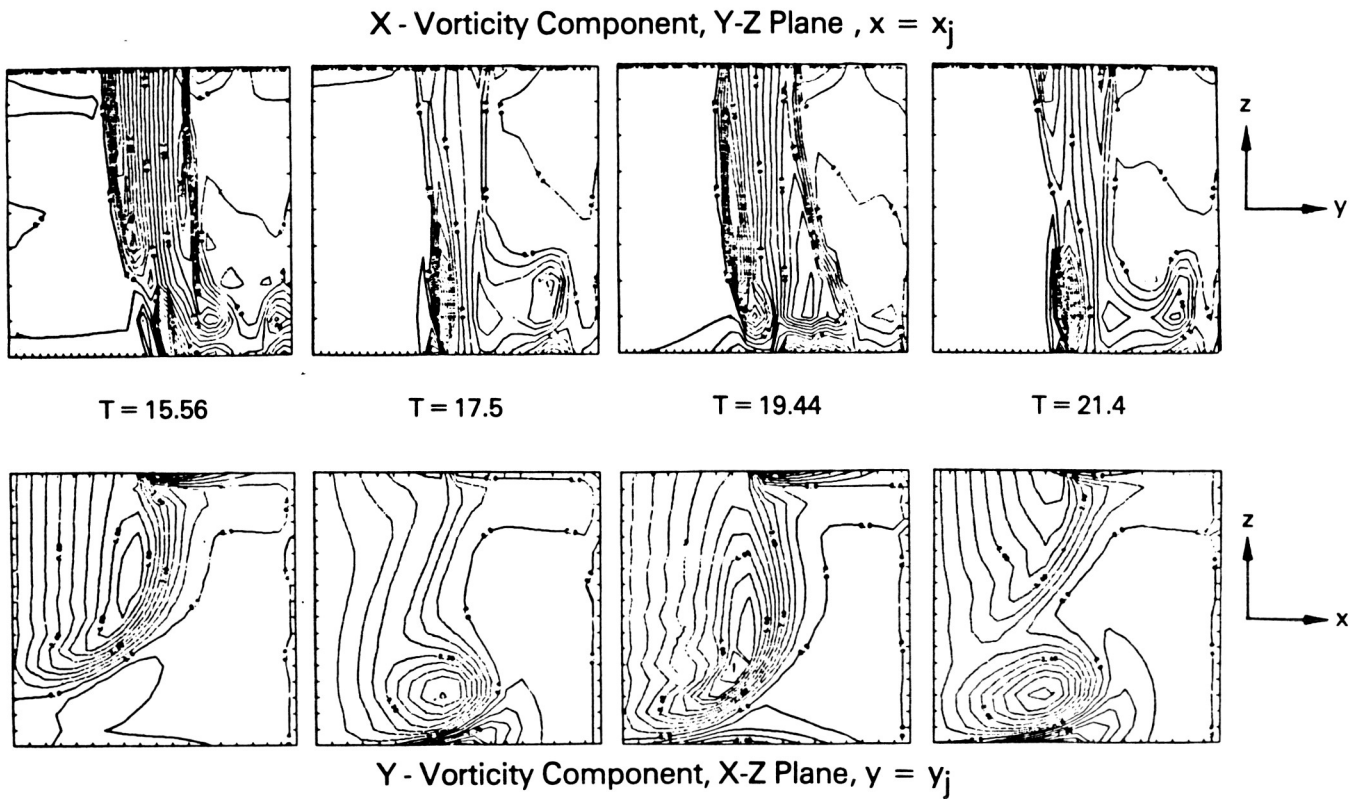
Figure 25.   Vorticity Contours for Profile I at Re = 300 with 40% Crossflow and Forced Axisymmetrically at St = 0.3

a. X - Vorticity Component, Y-Z Plane , x = x_j
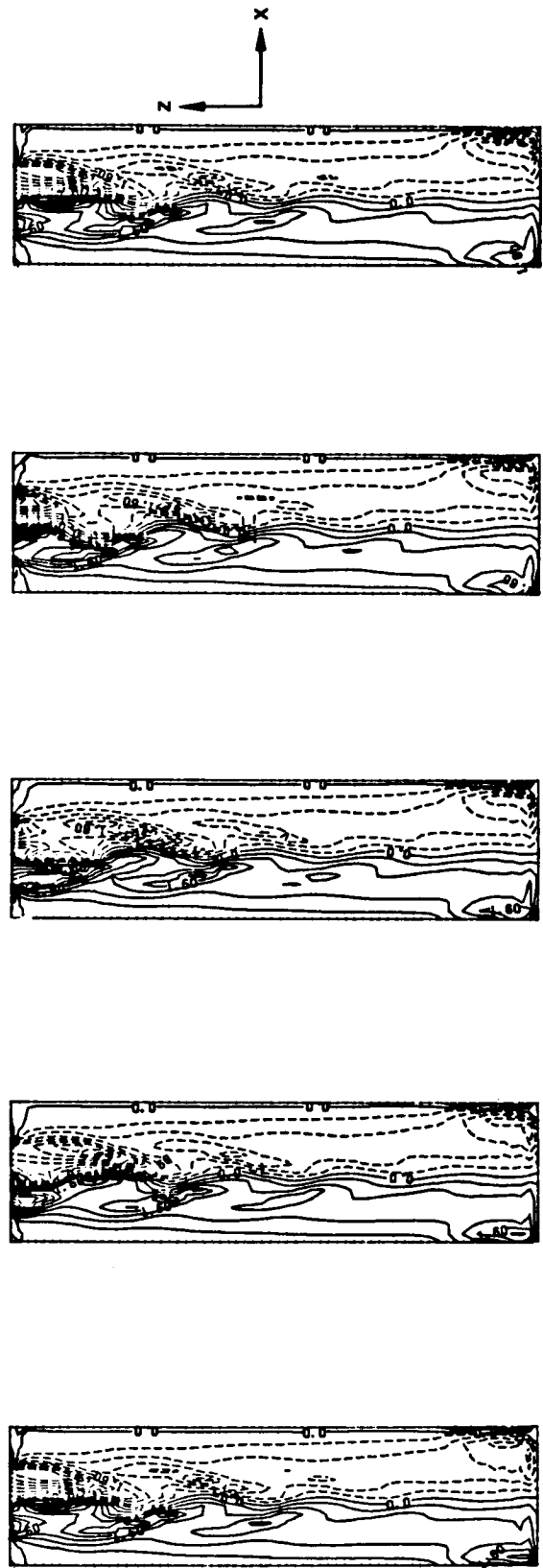
b. Y - Vorticity Component, X-Z Plane, y = y_j
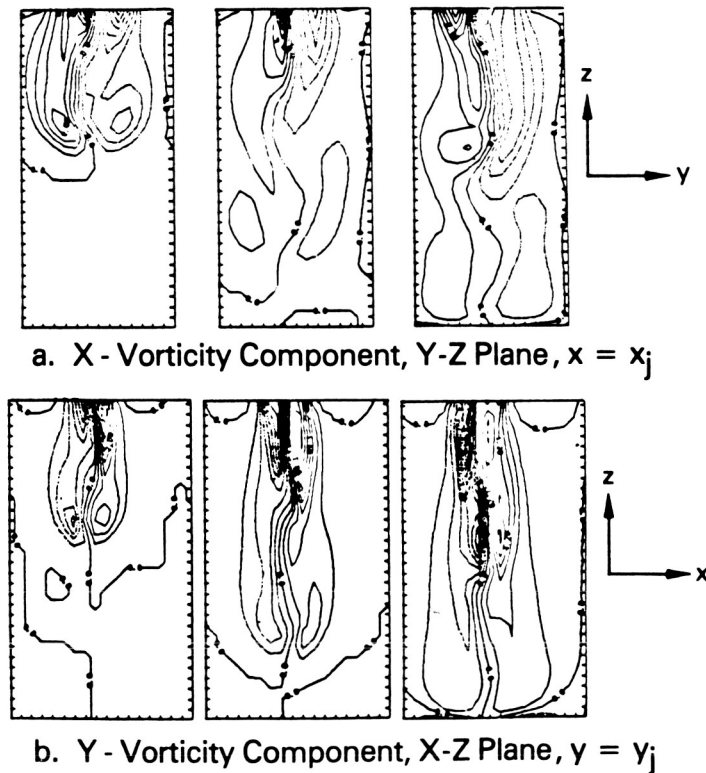
Figure 26.   Vorticity Contours for Profile I at Re = 100 and Forced Helically (Azimuthal Variation) at St = 0.165

X - Vorticity Component, Y-Z Plane, x = x_j

Y - Vorticity Component, X-Z Plane, y = y_j

a. T = 37.2, θ = 0

b. T = 37.97, θ = π/2

c. T = 38.81, θ = π

d. T = 39.6, θ = 3π/2

e. T = 40.47, θ = 2π

Figure 27. Vorticity Contours for Profile I at Re = 300 and Forced Helically (Azimuthal Variation) at St = 0.3. Plots Every π/2 of the Seventh Period

193